The Chemical Structure of Young High-mass Star-forming Clumps. II. Parsec-scale CO Depletion and Deuterium Fraction of HCO$^+$

S. Feng (冯思轶)[1,2,3] , D. Li[1,4] , P. Caselli[5] , F. Du[6,7] , Y. Lin[8] , O. Sipilä[5] , H. Beuther[9] , Patricio Sanhueza[3] ,
K. Tatematsu[10,11] , S. Y. Liu[2] , Q. Zhang[12] , Y. Wang[9] , T. Hogge[13] , I. Jimenez-Serra[14] , X. Lu[3] , T. Liu[15] ,
K. Wang (王科)[16] , Z. Y. Zhang[17] , S. Zahorecz[3,18] , G. Li[19] , H. B. Liu[2] , and J. Yuan[1]

[1] National Astronomical Observatories, Chinese Academy of Science, Beijing 100101, People's Republic of China; siyi.s.feng@gmail.com
[2] Academia Sinica Institute of Astronomy and Astrophysics, No. 1, Section 4, Roosevelt Road, Taipei 10617, Taiwan, Republic of China
[3] National Astronomical Observatory of Japan, National Institutes of Natural Sciences, 2-21-1 Osawa, Mitaka, Tokyo 181-8588, Japan
[4] NAOC-UKZN Computational Astrophysics Centre, University of KwaZulu-Natal, Durban 4000, South Africa
[5] Max-Planck-Institut für Extraterrestrische Physik, Gießenbachstraße 1, D-85748 Garching bei München, Germany
[6] Purple Mountain Observatory and Key Laboratory of Radio Astronomy, Chinese Academy of Sciences, Nanjing 210033, People's Republic of China
[7] School of Astronomy and Space Science, University of Science and Technology of China, Hefei, Anhui 230026, People's Republic of China
[8] Max Planck Institute for Radio Astronomy, Auf dem Hügel 69, D-53121 Bonn, Germany
[9] Max-Planck-Institut für Astronomie, Königstuhl 17, D-69117 Heidelberg, Germany
[10] Nobeyama Radio Observatory, National Astronomical Observatory of Japan, National Institutes of Natural Sciences, Nobeyama, Minamimaki, Minamisaku, Nagano 384-1305, Japan
[11] Department of Astronomical Science, SOKENDAI (The Graduate University for Advanced Studies), 2-21-1 Osawa, Mitaka, Tokyo 181-8588, Japan
[12] Center for Astrophysics | Harvard & Smithsonian, 60 Garden Street, Cambridge, MA 02138, USA
[13] Institute for Astrophysical Research, Boston University, Boston, MA 02215, USA
[14] Centro de Astrobiología (CSIC, INTA), Ctra. de Torrejón a Ajalvir km. 4, Torrejón de Ardoz, E-28850 Madrid, Spain
[15] Shanghai Astronomical Observatory, Chinese Academy of Sciences, 80 Nandan Road, Shanghai 200030, People's Republic of China
[16] Kavli Institute for Astronomy and Astrophysics, Peking University, 5 Yiheyuan Road, Haidian District, Beijing 100871, People's Republic of China
[17] School of Astronomy and Space Science, Nanjing University, 163 Xianlin Avenue, Nanjing 210023, People's Republic of China
[18] Department of Physical Science, Graduate School of Science, Osaka Prefecture University, 1-1 Gakuen-cho, Naka-ku, Sakai, Osaka 599-8531, Japan
[19] South-Western Institute for Astronomy Research, Yunnan University, Kunming, Yunnan 650500, People's Republic of China

Abstract

The physical and chemical properties of cold and dense molecular clouds are key to understanding how stars form. Using the IRAM 30 m and NRO 45 m telescopes, we carried out a Multiwavelength line-Imaging survey of the 70 μm-dArk and bright clOuds (MIAO). At a linear resolution of 0.1–0.5 pc, this work presents a detailed study of parsec-scale CO depletion and HCO$^+$ deuterium (D-) fractionation toward four sources (G11.38+0.81, G15.22–0.43, G14.49–0.13, and G34.74–0.12) included in our full sample. In each source with $T < 20$ K and $n_H \sim 10^4$–10^5 cm^{-3}, we compared pairs of neighboring 70 μm bright and dark clumps and found that (1) the H$_2$ column density and dust temperature of each source show strong spatial anticorrelation; (2) the spatial distribution of CO isotopologue lines and dense gas tracers, such as 1–0 lines of H^{13}CO$^+$ and DCO$^+$, are anticorrelated; (3) the abundance ratio between C^{18}O and DCO$^+$ shows a strong correlation with the source temperature; (4) both the C^{18}O depletion factor and D-fraction of HCO$^+$ show a robust decrease from younger clumps to more evolved clumps by a factor of more than 3; and (5) preliminary chemical modeling indicates that chemical ages of our sources are $\sim 8 \times 10^4$ yr, which is comparable to their free-fall timescales and smaller than their contraction timescales, indicating that our sources are likely dynamically and chemically young.

1. Introduction

The initial conditions of high-mass star formation (HMSF) are still under debate (e.g., Beuther et al. 2007; Tan et al. 2014; Motte et al. 2018; Sanhueza et al. 2019). For example, how different are the kinematics and chemical evolution during the formation of high-mass star clusters with respect to their low-mass analogs? In particular, what is the chemical environment of these high-mass clumps (e.g., Sanhueza et al. 2012; Feng et al. 2016a; Tatematsu et al. 2017)? How do gas motions (e.g., infall, outflow) link the parental clouds and the descendant high-mass clumps during star formation (e.g., Wang et al. 2014; Beuther et al. 2015; Zhang et al. 2015; Sanhueza et al. 2017; Contreras et al. 2018; Lu et al. 2018)? Two steps are essential to address these questions (e.g., Zhang et al. 2009): (1) identifying the "initial" environments that have the potential to form high-mass stars and (2) precisely characterizing the chemical and kinematic properties of these "initial" environments from the observations.

The dense ($n > 10^3$–10^5 cm^{-3}; Rathborne et al. 2006), cold ($T < 20$ K; Wang et al. 2012), and less luminous infrared-dark molecular clouds (IRDCs) are of particular interest (e.g., Sanhueza et al. 2013; Tan et al. 2013). In particular, the 70 μm dark (Dunham et al. 2008) high-mass clumps, with bolometric luminosity (L_{bol})–to–mass (M_c) ratios less than 1 $L_\odot/M_\odot$ (Molinari et al. 2016), are prime targets for studying initial conditions. These regions may contain clusters of low-mass young stellar objects or be prestellar and thus future sites of intermediate-/high-mass protostellar objects. Therefore, they are excellent space laboratories to test not only the chemical processes in the cold and dense environment but also different kinematic scenarios of HMSF (e.g., competitive accretion, Bonnell et al. 2004; Bonnell & Bate 2006; or monolithic collapse, McKee & Tan 2003; Krumholz et al. 2005, 2009).

Previous multiwavelength dust continuum surveys have provided several catalogs of initial HMSF clump candidates (e.g., Ragan et al. 2012; Guzmán et al. 2015; Svoboda et al. 2016; Yuan et al. 2017). However, observations of the dust continuum can discern neither the kinematic nor chemical properties of these candidates. Since these properties are crucial to understanding the high-/intermediate-/low-mass star formation in high-mass clumps, spectroscopic images with a high spatial dynamic range (0.01–1 pc) and fine velocity resolution are essential for these properties.

To characterize the chemical processes and gas motions in the early phase of high-mass clumps, we designed and carried out the Multiwavelength line-Imaging survey of the 70 μm-dArk and bright clOuds (MIAO[20]) project (see Section 2.1). Given that the data collected for this project have a broad range of spatial and spectral coverage, we plan to carry out a series of analyses on the detailed chemistry (this work; S. Feng et al. 2020, in preparation, hereafter Papers IV and V) and kinematics (S. Feng et al. 2020, in preparation, hereafter Paper III) of our source sample.

In the present work, we focus on two crucial chemical processes in early star-forming environments, when molecular clouds are cold ($T < 20$ K) and dense ($n > 10^4$ cm^{-3}), namely, freeze-out and deuterium (D-) fractionation (e.g., Caselli et al. 2002a).

Freeze-out is the process that allows gaseous species, including elements heavier than He, to adsorb on the surface of dust grains (e.g., Aikawa 2013). The D-fractionation of gas-phase species is a process that starts by unlocking atomic deuterium from HD through cosmic ray–driven ion–molecule chemistry (e.g., Millar et al. 1989; Ceccarelli et al. 2014). Isotope exchange reactions take place via H_3^+, yielding H_2D^+, D_2H^+, and D_3^+ (e.g., Caselli et al. 2002b; Crapsi et al. 2005; Vastel et al. 2006; Chen et al. 2010), which then react with more abundant species, such as CO and N_2, to produce species such as DCO^+ and N_2D^+.

Observationally, CO freeze-out (also called CO depletion) is measured as the ratio of the expected CO canonical abundance with respect to its observed gaseous abundance. Depletion of CO has been widely detected toward cold and dense starless clumps and cores (e.g., Willacy et al. 1998; Caselli et al. 1999; Kramer et al. 1999; Bergin et al. 2002; Bacmann et al. 2003; Fontani et al. 2012), where the CO depletion peaks show spatial coincidence with the D-fractionation peaks of gas-forming species, such as N_2H^+ and HCO^+. In most cases, such a spatial coincidence appears at a subparsec spatial scale (e.g., Caselli et al. 1999). Recent observations have revealed parsec-scale CO depletion (Hernandez et al. 2011; Giannetti et al. 2014; Sabatini et al. 2019) associated with high D-fractionation (e.g., Barnes et al. 2016; Feng et al. 2019). However, cases of parsec-scale CO depletion are much more rarely reported than subparsec-scale cases. One reason is that the history of studying IRDCs is relatively short. In particular, IRDCs that are 70 μm dark are mostly, if not entirely, identified with the Herschel Space Observatory, which was launched only about a decade ago. Due to a lack of candidates, the chance of witnessing parsec-scale CO depletion toward the star-forming regions at the extreme young stage (dense and with a short timescale) are small. Another reason is that, to identify CO

depletion, adequate linear resolution is crucial, for high-depletion zones are localized in relatively small, low-temperature, and high-density regions. Millimeter/submillimeter interferometers offer sufficient resolutions, but CO data are hampered by missing fluxes due to their large spatial extent. Although observations from single-dish telescopes are not affected by missing fluxes, many of them offer too limited angular resolutions to probe the densest region. Moreover, imaging a large field at adequately high spatial resolution and spectral sensitivity required good weather conditions and was very time-consuming.

By taking advantage of new, high-sensitivity observational instrumentation, we carried out a line-imaging survey project on a large sample of sources. In Section 2, we introduce our MIAO survey project and summarize the observations and data quality. We present the maps of continuum and molecular line emission toward a pilot sample of four regions in Section 3.1 and characterize their physical structures in Section 3.2. In Section 4, we discuss the possible spatial relation between the CO depletion factor, D-fraction of HCO^+, source temperature, and density toward each region, as well as fit our chemical model to the observations. Finally, a summary of our main results can be found in Section 5.

2. Survey Design and Observations

2.1. MIAO

During 2016–2017, we carried out a pilot line-imaging survey toward the filamentary IRDC G28.34+0.06 (e.g., Wang 2018). Using the Institut de Radio Astronomie Millimétrique 30 m telescope (IRAM 30 m), we comparatively observed G28.34 P1-S, a pair of 70 μm bright and dark dense clumps separated at a subparsec distance in this IRDC at 1–4 mm wavelength. On the one hand, we unveiled varying degrees of high-mass star-forming activities from prestellar to protostellar objects, such as parsec-scale infall signatures (Feng et al. 2016a) and dynamically extremely young outflows ($\sim 10^4$ yr; Feng et al. 2016b; Tan et al. 2016; Kong et al. 2018). On the other hand, we also revealed the chemical variations in the framework of evolutionary stages of star formation, such as parsec-scale CO depletion (Feng et al. 2016a) and species-dependent D-fractionation (Feng et al. 2019; Paper I).

However, we cannot generalize our conclusions because of the small sample size. To ground our pilot study results, we initiated a multiwavelength line-imaging survey project (MIAO) in 2017. Aiming to characterize the chemical processes (presented here) and gas motions (S. Feng et al. 2020, in preparation) in primordial high-mass clumps, we designed this project to observe a sample of 24 extremely cold, dense clumps (Table A1) by using the IRAM 30 m, the Nobeyama 45 m telescope (NRO 45 m), and the Atacama Large Millimeter/submillimeter Array (ALMA). To have a robust analysis, we select the sources in the sample based on the following criteria.

1. *Dense.* All of the regions in our sample are selected from a high-mass starless clump (HMSC) candidate catalog (Yuan et al. 2017), which is provided by analyzing the millimeter and submillimeter continuum from the APEX/ATLASGAL (Schuller et al. 2009), Spitzer/GLIMPSE–MIPSGAL (Benjamin et al. 2003; Churchwell et al. 2010), and Herschel/Hi-GAL (Molinari et al. 2010) surveys throughout the entire inner Galactic plane. For

---

[20] "MIAO" shares a pronunciation with three Chinese characters: a noun ("the seed or something in the initial condition"), an adjective ("wonderful"), and a verb ("to draw the profile of something").

Table 1
Sources in This Work and Their Observation Parameters

Source[a]	Abbrev.	R.A.[b] (J2000)	Decl.[b] (J2000)	d[c] (kpc)	R_{GC}[d] (kpc)	V_{sys} (km s^{-1})	rms$_{4.0mm}$[e] (K)	rms$_{3.4mm}$[f] (K)	rms$_{1.3mm}$[g] (K)	rms$_{2.7mm}$[h] (K)
G015.2169−0.4267	G15.22−0.43	$18^h19^m51^s\!.2$	$-15°54'50''\!.8$	1.9	6.1	22.7[i]	0.05	0.04	0.33	0.26
G011.3811+0.8103	G11.38+0.81	$18^h07^m36^s\!.4$	$-18°41'21''\!.1$	2.8	5.2	26.8[j]	0.02	0.02	0.17	0.24
G014.4876−0.1274	G14.49−0.13	$18^h17^m19^s\!.0$	$-16°24'53''\!.6$	3.2	4.9	39.7[k]	0.03	0.03	0.31	0.46
G034.7391−0.1197	G34.74−0.12	$18^h55^m09^s\!.7$	$+01°33'13''\!.3$	4.7	5.2	79.0[l]	0.02	0.02	0.18	0.22

Notes.
[a] ATLASGAL name. A complete list of sources in our sample is given as Appendix Table A1.
[b] OTF mapping center.
[c] Kinematic distance, from Yuan et al. (2017), with an uncertainty of ±0.5 kpc.
[d] Galactocentric distance, calculated by using Wenger et al. (2018).
[e] Measured by IRAM 30 m in main-beam temperature T_{mb} (K) directly from observations without smoothing, with an angular resolution of ∼36″ and velocity resolution of ∼0.72 km s^{-1} for 4.0 mm lines.
[f] Measured by IRAM 30 m in main-beam temperature T_{mb} (K) directly from observations without smoothing, with an angular resolution of ∼29″ and velocity resolution of ∼0.56 km s^{-1} for 3.4 mm lines.
[g] Measured by IRAM 30 m in main-beam temperature T_{mb} (K) directly from observations without smoothing, with an angular resolution of ∼11″ and velocity resolution of ∼0.22 km s^{-1} for 1.3 mm lines.
[h] Measured by NRO 45 m in main-beam temperature T_{mb} (K) directly from observations without smoothing, with an angular resolution of ∼16″ and velocity resolution of ∼0.12 km s^{-1} for 2.7 mm lines.
[i] Dempsey et al. (2013).
[j] Csengeri et al. (2014).
[k] Wienen et al. (2012).
[l] Shirley et al. (2013).

comparative study, each imaged region covered a pair of 70 μm dark and bright clumps. Both clumps in each region are high-mass, with $M > 870\,M_\odot\,(\text{radius/pc}^{-1})^{1.33}$ (Kauffmann & Pillai 2010) and mass surface density >0.2 g cm^{-2}, fulfilling the empirical threshold of 0.05 g cm^{-2} given by Urquhart et al. (2014) and He et al. (2015) for HMSF. Specifically, each 70 μm dark clump is an HMSC candidate with high dust extinction and low luminosity ($L_{bol}/M_c < 1\,L_\odot/M_\odot$; Molinari et al. 2016), and it is associated with neither a methanol maser nor an H II region, indicating that they are young.

2. *Cold.* Using the spectral energy distribution (SED) method (elaborated in Lin et al. 2017; Yuan et al. 2017; and Section 3.2.1), the dust temperature of each 70 μm dark clump in our sample is low (<20 K).

3. *Relatively near.* The sources in our sample are selected within a kinematic distance of $d < 5$ kpc. At an angular resolution from 30″ (IRAM 30 m observations) down to 2″ (ALMA observations), a quantitative characterization of the star-forming activities at a subparsec linear resolution will help us interpret the star-forming activities of more distant regions.

4. *Well-constrained environmental properties of the parental cloud.* Each 70 μm dark clump is located at the morphological end of a filamentary cloud. Such objects have been proposed as prime targets to study the initial conditions of HMSF because gravity-driven accretion (gravitational acceleration) is likely enhanced around the morphological ends of the filaments and in the edges of sheetlike structures (edge effects) on a timescale shorter than the global collapse timescale (e.g., Burkert & Hartmann 2004; Pon et al. 2012; Li et al. 2016). At least one 70 μm bright counterpart is within a $1'\!.5$ (<2 pc) distance to the 70 μm dark clump in the plane of the sky. Pairs of 70 μm dark and bright clumps show the same

systemic velocity V_{sys} as previous point observations by using single-dish telescopes (Purcell et al. 2012; Wienen et al. 2012; Dempsey et al. 2013; Shirley et al. 2013; Csengeri et al. 2014), indicating that they are in the same parental cloud. Being away from the filament ends, the 70 μm bright clump may be dynamically more evolved than the 70 μm dark clump.

Our comparative kinematic and chemical study toward the 70 μm dark and bright clump pairs in each region includes the comparison of molecular line profiles, molecular spatial distributions, and relative abundances between different species. Such a study will minimize environmental differences (e.g., interstellar UV heating, cosmic-ray ionization rate (CRIR), elemental abundances, magnetic fields), which goes a step ahead of previous studies that targeted samples of spatially separated sources in different clouds.

The present work focuses on the parsec-scale chemical features, and the data were obtained from the following single-dish observations.[21]

2.2. IRAM 30 m Observations

The line-imaging survey of the entire sample of 24 regions was carried out using the IRAM 30 m telescope at 1.3, 3.4, and 4.0 mm. Observations were performed in on-the-fly (OTF) mode from 2017 August to 2018 May, and the map centers of the four sources considered in the present work are listed in Table 1 (see the complete list of the entire sample in Table A1).

The broad bandpass of EMIR simultaneously covers 16 GHz bandwidth. By superpositioning two spectral tunings, our observations cover the frequency ranges 70.718–78.501, 82.058–94.183, and 217.122–224.842 GHz in total. These

---

[21] Our ongoing ALMA observations will be presented in a future study (Paper III), focusing on the connection between the parsec- and subparsec-scale gas motions (S. Feng et al. 2020, in preparation).

frequency ranges cover several dense gas tracers, shock tracers, and deuterated lines (see the targeted lines in Table A2, which will be analyzed in future studies). Using the FTS200 backend, we achieve a frequency resolution of 195 kHz (corresponding to 0.659 km s^{-1} at 88.632 GHz). The angular resolution of the IRAM 30 m telescope is $29\rlap{.}''3$ at 88.632 GHz. The weather conditions during the observations were good (radiometer opacity τ at 255 GHz < 0.6), and we used Saturn and Mars for pointing and focus. Using the corresponding forward efficiency ($F_{\rm eff}$) and a main-beam efficiency ($B_{\rm eff}$) at individual frequencies,[22] we converted the data from antenna temperature (T_A^*) to main-beam temperature ($T_{\rm mb} = F_{\rm eff}/B_{\rm eff} \times T_A^*$). We used the GILDAS software package for data reduction and line identification. The typical rms noise levels in $T_{\rm mb}$ in the line-free channels are listed in Table 1.

2.3. NRO 45 m Observations

Using the FOREST receiver (Minamidani et al. 2016) mounted on the NRO 45 m telescope, our entire sample was observed with the NRO 45 m telescope from 2018 January to 2018 February, simultaneously targeting the ground transition lines of C^{18}O, C^{17}O, and ^{13}CO. Employing the OTF scan mode (Sawada et al. 2008), each region was imaged with the same map size and center as those in the IRAM 30 m observations (Table A1).

Using the SAM45 digital spectrometer (Kamazaki et al. 2012), we achieved a frequency resolution of 61.04 kHz (corresponding to 0.120 km s^{-1} at 109.783 GHz). The effective angular resolution, i.e., FWHM beam of the NRO 45 m is $16\rlap{.}''4$ at 109.783 GHz.

The telescope pointing was established by observing the 43 GHz SiO maser of OH397 or VX-SGR every 60 minutes, achieving an accuracy of $\sim 5''$ (FWHM beam as $42''$ at 43 GHz). Using the corresponding main-beam efficiency $\eta_{\rm mb}$ (44% $\pm$ 3% at 110 GHz), we converted the data from antenna temperature (T_A^*) to main-beam temperature ($T_{\rm mb} = T_A^*/\eta_{\rm mb}$). We used the NOSTAR software package (Sawada et al. 2008) for data reduction. The rms noise levels in $T_{\rm mb}$ in the line-free channels are listed in Table 1.

2.4. Archival Data

Moreover, we used the following archival data.

Continuum data were obtained from the Herschel/Hi-GAL survey at 160 μm (PACS) and 250, 350, and 500 μm (SPIRE; Molinari et al. 2010), as well as from the combination of Planck (Planck Collaboration et al. 2014) and James Clerk Maxwell telescope (JCMT) SCUBA2 data at 850 μm (G11.38 +0.81 and G14.49–0.13; ObsID: M11BEC30) or APEX-LABOCA data at 870 μm (G15.22–0.43 and G24.74–0.12; Schuller et al. 2009).

We also used NH$_3$ (J, K) = (1, 1) and (2, 2) lines from the Radio Ammonia Mid-plane Survey (RAMPS; Hogge et al. 2018), observed with the Green Bank Telescope (GBT). The data achieve an angular resolution of $\sim 34\rlap{.}''7$ and a velocity resolution of 0.018 km s^{-1}. Using a main-beam efficiency of 0.91, the rms in $T_{\rm mb}$ for each source is ~ 0.5 K.

---

[22] http://www.iram.es/IRAMES/mainWiki/Iram30mEfficiencies

3. Results and Analysis

3.1. Spatial Distribution of the Continuum and Molecular Line Emission

Analyzing our entire sample of 24 regions, we found that over 50% show parsec-scale CO depletion. A complete statistical overview of the chemical and physical properties of the entire sample will be given in a follow-up paper. Grouping these sources according to their kinematic distances (d) progressively further away from the Sun, we picked out a pilot sample of four regions (G11.38+0.81, G14.49–0.13, G15.22–0.43, and G34.74–0.12) that show the most obvious spatial anticorrelation between CO and deuterated species from each kinematic distance group.

All four regions in the pilot sample contain a clump, for which the 70 μm extinction and 870 μm emission are spatially correlated (P1 in Figure 1, left). This indicates that these 70 μm dark clumps are at an early stage in their evolution.

In each region, extracting the beam-averaged spectrum toward the 870 or 70 μm continuum peaks, we found that, at a linear resolution of >0.1 pc, neighboring clumps in the same cloud show similar line profiles (Figures A1), i.e., the differences in the centroid velocities and FWHM line widths toward neighboring clumps are less than 2 km s^{-1} (Table A3).

To compare the chemical differentiations of molecules in the same clouds, it is important to have the spatial distribution maps of all of the molecular lines covered by our multi-wavelength line-imaging survey project (listed in Table A2). Considering their broad line widths (FWHM $\sim$ 2–6 km s^{-1}), we imaged their integrated intensities over the same velocity range toward each source, covering all of the line wings down to the continuum level (given in Table A3). In particular, lines with critical densities >10^5 cm^{-3} in the temperature range of 10–20 K are treated as high-density tracers, including the 1–0 lines from HCN isotopologues (H^{13}CN, HC^{15}N, DCN), HNC isotopologues (HN^{13}C, H^{15}NC, DNC), HCO$^+$ isotopologues (H^{13}CO$^+$, HC^{18}O$^+$, DCO$^+$), and N$_2$H$^+$ isotopologues (N$_2$D$^+$), which are covered by our observations (Table A2). Morphologically, they are spatially coincident with the 870 μm continuum emission. In contrast, the integrated intensities of the 1–0 and 2–1 lines from C^{17}O, ^{13}CO, and C^{18}O show anticorrelated spatial distributions with the dense gas tracers, as already found in low-mass star-forming regions (e.g., Caselli et al. 2002a).

We focus here on the spatial distributions of C^{18}O(2–1) and DCO$^+$(1–0) toward each source, based on the consideration of the observational uncertainties, chemical differentiation, and data sensitivity. (1) Comparing the data obtained from the same observations will exclude the uncertainty of pointing and calibration caused by using two different telescopes, so we do not show the 1–0 lines of CO isotopologues obtained from the NRO 45 m here. (2) Theoretically, N$_2$H$^+$ and HCO$^+$ are formed exclusively in the gas phase (e.g., Parise et al. 2002; Aikawa et al. 2005, 2012; Graninger et al. 2014). Emission intensity peaks of N$_2$D$^+$(1–0) and DCO$^+$(1–0) are strong indicators of the densest and coldest environment of each source. This has been proved by extensive observations, including our pilot study (e.g., Fontani et al. 2014; Feng et al. 2019). (3) Investigating the line profiles of the dense gas tracers and CO isotopologue lines (Figure A1), we found that the signal-to-noise ratios (S/Ns) of C^{17}O(2–1) and N$_2$D$^+$(1–0) are
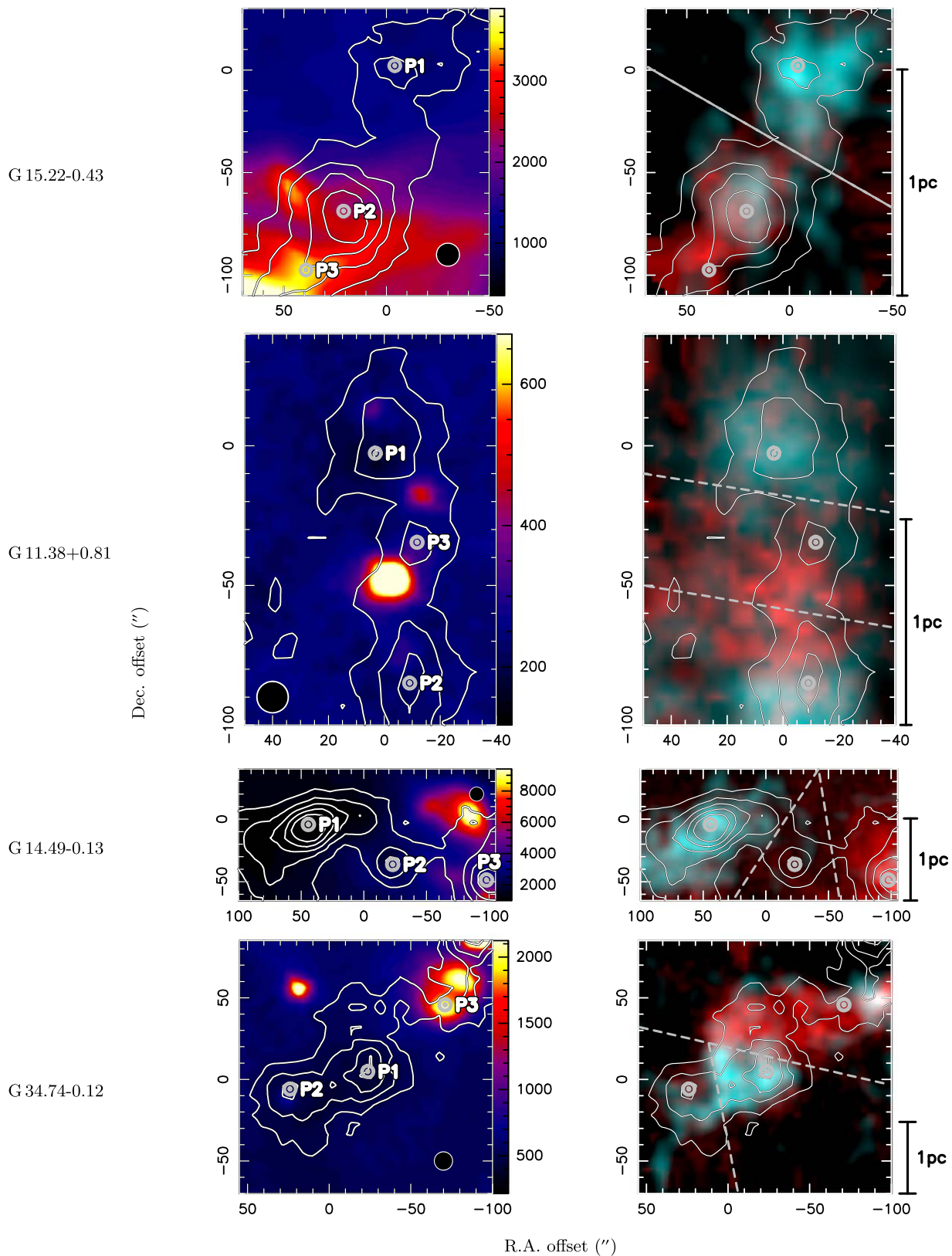
Figure 1. Compilation of the continuum and line data for G15.22–0.43, G11.38+0.81, G14.49–0.13, and G34.74–0.12. Left column: color maps of the dust emission observed by Herschel at 70 μm (colorscale in units of MJy sr^{-1}). Right column: two-color maps show the intensity of C^{18}O (2–1; in red and with an angular resolution of $11\rlap{.}{''}8$) and DCO^{+}(1–0; in cyan and with an angular resolution of $36\rlap{.}{''}0$) integrated in the same velocity range (given in Table A3). The white contours in each panel show continuum emission observed by APEX at 870 μm (Schuller et al. 2009), starting from 3σ rms and increasing by 3σ steps. The 1σ of 870 μm emission for G15.22–0.43, G11.38+0.81, G14.49–0.13, and G34.74–0.12 is 15.2, 10.6, 23.7, and 20.6 MJy sr^{-1}, respectively, at an angular resolution of $18\rlap{.}{''}2$ (shown in black in the corners of the left panels). The dashed lines and the labeled positions P1, P2, and P3 in each panel are described in Section 3.1.

too low (S/N < 5) toward some regions, and that ^{13}CO(2–1) seems to be optically thick at certain locations.

For each region, the dust continuum emission at 70 and 870 μm is shown in the left panel of Figure 1, and a two-color image of C^{18}O(2–1) (red) and DCO$^+$(1–0) (cyan) is shown in the right panel of Figure 1. Comparing these two panels, we visually separate each source into two to three zones.

The DCO$^+$-dominant zone appears cyan in the two-color image, where C^{18}O emission is weaker than elsewhere. The 870 μm continuum peak in this region is labeled P1, where the dust emission at 70 μm is $<3\sigma$ rms.

The CO-dominant zone appears reddish in the two-color image, where the DCO$^+$(1–0) emission shows S/N < 3. This region is 70 μm bright, and we label the continuum peak at either 870 μm (if it exists; e.g., G14.49–0.13 and G11.38 +0.81) or 70 μm (e.g., G34.74–0.12 and G15.22–0.43) P3.

The transition zone exhibits equally weak (e.g., G34.74–0.12, G14.49–0.13) or strong (G11.38+0.81) DCO$^+$ and CO emission. The 870 μm continuum peak in this region is labeled P2, and the dust emission at 70 μm here is brighter than that toward P1. Since G15.22–0.43 shows only two continuum peaks at 870 μm in the imaged region, we do not separate the CO-dominant and transition zones on its map.

3.2. CO Depletion Factor and D-fraction of HCO$^+$

Following Feng et al. (2019), we derive the map of the CO depletion factor and the D-fraction map of HCO$^+$ for each source in four steps.

3.2.1. Dust Temperature Map and H$_2$ Column Density Map

Using our well-developed image combination and iterative SED fitting method (see details in Lin et al. 2016, 2017 and our pilot study, Feng et al. 2019, hereafter Paper I), we established a reliable blackbody model and obtained the dust opacity index β map for each source at a coarse angular resolution of 37″. In order to recover the missing flux of the parsec-scale structure, we used the continuum data from PACS 160 μm and SPIRE 250, 350, and 500 μm and combined the Planck data with JCMT at 850 μm or APEX at 870 μm.

Then, assuming that the β map has no local variation from 37″ to 18″ resolution and that the gas-to-dust mass ratio $\log(\gamma) = 0.087 R_{GC}$ (kpc) + 1.44 (Draine 2011; Giannetti et al. 2017a) changes with galactocentric distance R_{GC}, we fit the SED of each pixel by using the continuum data from PACS 160 μm, SPIRE 250 μm, and the combined PLANCK-JCMT 850 μm or PLANCK-APEX 870 μm. Therein, achieving an angular resolution of 18″ or 20″, we simultaneously obtain the maps of dust temperature T_{dust} and H$_2$ column density N_{H_2} (Figure 2).

The H$_2$ column density toward each clump is in the range of 10^{22}–10^{23} cm^{-2} (Table 2), which is at least 1 mag higher than that ($\sim 10^{21}$ cm^{-2}) toward the outskirts of the natal cloud (the location where the continuum emission at 870 μm is $<5\sigma$ rms). Therefore, we believe that the background and foreground contamination have a negligible effect on the H$_2$ column density estimates of our targeted regions.

3.2.2. Gas Temperature

Our line-imaging survey includes three thermometers: para (p)–NH$_3$ lines, p–H$_2$CO lines, and CO isotopologue lines.

The N-bearing species are resilient to depletion (e.g., Caselli et al. 1999; Bergin et al. 2002; Caselli et al. 2002b; Jørgensen et al. 2004). The inversion lines from different rotational ladders (J = 1, 2 ...) are coupled only collisionally and have similar frequencies. Furthermore, the combination of its energy level structures and the numerical value of Einstein coefficients A_{ij} makes the majority of the NH$_3$ population stay in the metastable states. In the temperature range of 10–100 K, inversion lines of NH$_3$ have modestly high critical densities of $\lesssim 10^4$ cm^{-3} (e.g., Ho & Townes 1983; Walmsley & Unger-echts 1983; Crapsi et al. 2007; Rosolowsky et al. 2008; Juvela & Ysard 2011). These unique qualities make NH$_3$ a great interstellar thermometer for the gases of modestly high (e.g., inversion lines; see Li 2002; Li et al. 2003) and high (e.g., rotational transition lines; see Caselli et al. 2017) densities. Two regions in our pilot sample (G14.49–0.13 and G34.74–0.12) are covered by the RAMPS program, so we use the p–NH$_3$ lines (J, K) = (1, 1) and (2, 2) to provide the gas temperature maps toward them. To derive the gas kinetic temperature T_{kin} (p–NH$_3$) maps at an angular resolution of 34″, we apply two Monte Carlo fitting tools; one is HfS, developed by Estalella (2017), and another is a much faster temperature-fitting algorithm (Wang et al. 2020).[23] We found consistent results for T_{kin} (p–NH$_3$) from both tools, spanning the range of 11–21 K in our pilot sample.

Comparing this gas temperature with the dust temperature T_{dust} (Section 3.2.1) toward P1, P2, and P3 of each region (Table 2), we found that they are consistent at individual positions, though the angular resolutions for their measurements are different. Therefore, we believe that dust and gas are thermally coupled in G14.49–0.13 and G34.74–0.12 (Goldsmith 2001). The NH$_3$ images toward G15.22–0.43 and G11.38 +0.81 are not available. Nevertheless, they show similar dust properties (dynamic ranges of T_{dust} and N_{H_2}) as the other two, so we expect that the dust and gas toward these regions are thermally coupled as well, i.e., the T_{kin} (p–NH$_3$) maps of G15.22–0.43 and G11.38+0.81 are consistent with their T_{dust} maps.

Using the IRAM 30 m and NRO 45 m, we observed the 1–0 and 2–1 lines of all three CO isotopologues (C^{18}O, C^{17}O, and ^{13}CO) at an angular resolution of 16″ and 12″, respectively. Smoothing them to the same angular resolution as that of the dust continuum observations (18″ or 20″) allows us to compare the gas and dust temperature at the same spatial scale toward individual regions. To test whether these low-J lines can be treated as gas thermometers in each region, we estimate the H and H$_2$ number density n_H, the molecular column density N_{mol}, and the gas kinetic temperature T_{kin} (CO) toward P1, P2, and P3 by employing the large velocity gradient (LVG) escape probability approximation. Using the non-local thermal equilibrium (non-LTE) statistical equilibrium radiative transfer code RADEX (van der Tak et al. 2007), along with a related solver (Fujun Du's myRadex),[24] we apply the MultiNest Algorithm (Feroz & Hobson 2008; Feroz et al. 2009, 2019) and derive the probability density function (PDF) of these variables (Table 2). From the best-fit results, the T_{kin} (CO) toward individual locations in G15.22–0.43 and G14.49–0.13 is

---

[23] This tool is to measure the gas kinetic temperature by only using the line intensity ratios between NH$_3$ hyperfine groups, which was first proposed by Li et al. (2013). The python package for this method (Wang et al. 2020) is publicly available at https://github.com/plotxyz/nh3_trot.git.

[24] See https://github.com/fjdu/myRadex.
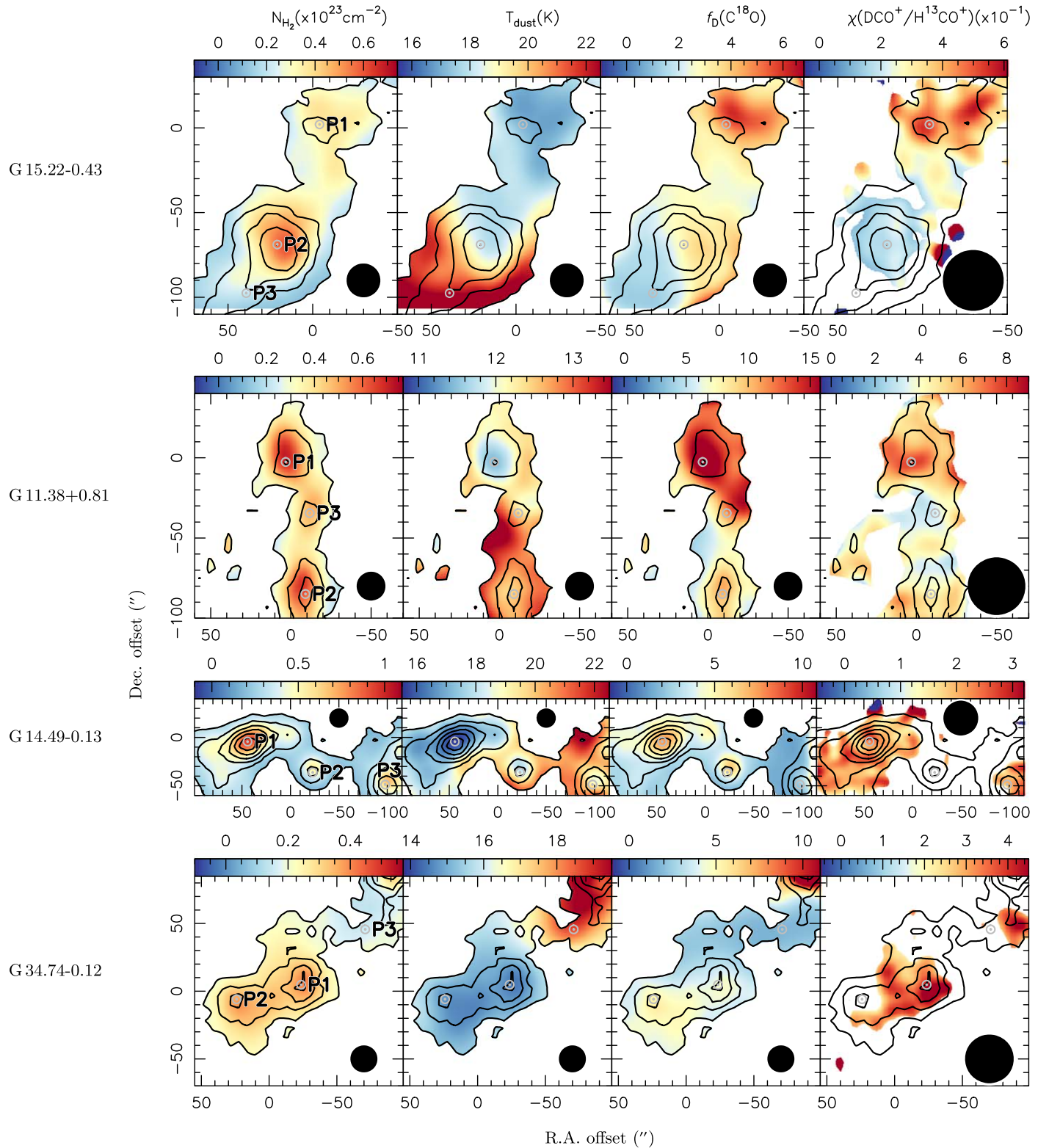
Figure 2. Color maps of H$_2$ column density (first column) and dust temperature from SED fitting (second column), C^{18}O depletion factor (third column), and relative abundance ratio between DCO$^+$ and H^{13}CO$^+$ (fourth column) toward regions G15.22–0.43, G11.38+0.81, G14.49–0.13, and G34.74–0.12. The black contours show continuum emission observed by APEX at 870 μm (Schuller et al. 2009), with the contour levels as in Figure 1. The blanking threshold for the first to third panels is <3σ continuum emission at 870 μm; for the fourth panel, it is the pixels where DCO$^+$(1–0) shows <3σ emission. The angular resolution for each map is given in the top or bottom right corner by the black circles.

generally higher than T_{dust} but with larger uncertainties (20%–50%). A possible reason might be the deeply embedded protostellar objects and young outflows, which have been resolved with our ALMA observations at higher angular resolution (1″2; Li et al. 2019; Sanhueza et al. 2019; S. Feng et al. 2020, in preparation). In contrast, the T_{kin} (CO) toward

Table 2
Dust and Gas Properties of Our Target

Properties	Source[a]	G15.22–0.43	G11.38+0.81	G14.49–0.13	G34.74–0.12
[R.A., Decl.][a] (J2000, J2000)	P1	[$18^h19^m52^s.637$, $-15°55'59''.95$]	[$18^h07^m35^s.771$, $-18°42'46''.37$]	[$18^h17^m16^s.750$, $-16°25'21''.33$]	[$18^h55^m12^s.803$, $+01°33'01''.75$]
	P2	[$18^h19^m50^s.907$, $-15°54'49''.07$]	[$18^h07^m36^s.638$, $-18°41'24''.05$]	[$18^h17^m22^s.106$, $-16°24'58''.51$]	[$18^h55^m09^s.624$, $+01°33'12''.44$]
	P3	[$18^h19^m53^s.907$, $-15°56'28''.66$]	[$18^h07^m35^s.584$, $-18°41'55''.96$]	[$18^h17^m12^s.229$, $-16°25'42''.85$]	[$18^h55^m06^s.466$, $+01°33'53''.34$]
N_{H_2}[b] ($\times10^{22}$ cm^{-2})	P1	3.6 ± 0.1	6.7 ± 0.1	9.3 ± 0.8	3.9 ± 0.2
	P2	5.5 ± 0.1	5.9 ± 0.1	4.6 ± 0.2	3.7 ± 0.1
	P3	2.1 ± 0.1	4.7 ± 0.1	5.8 ± 0.1	1.6 ± 0.1
T_{dust}[b] (K)	P1	17.2 ± 0.1	11.5 ± 0.1	15.6 ± 0.3	14.6 ± 0.1
	P2	17.9 ± 0.1	12.6 ± 0.1	18.0 ± 0.2	14.9 ± 0.1
	P3	21.9 ± 0.1	12.2 ± 0.1	18.9 ± 0.1	18.8 ± 0.1
T_{kin} (p–NH$_3$)[e] (K)	P1	$\cdots$[c]	$\cdots$[c]	16.1 ± 0.9	14.9 ± 1.7
	P2	$\cdots$[c]	$\cdots$[c]	17.9 ± 5.6	13.3 ± 1.0
	P3	$\cdots$[c]	$\cdots$[c]	17.1 ± 6.5	15.8 ± 3.5
T_{kin} (p–H$_2$CO)[f] (K)	P1	25.2 ± 1.5	27.5 ± 14.0	22.7 ± 1.5	28.0 ± 1.9
	P2	25.5 ± 1.5	37.6 ± 3.9	19.6 ± 12.4	20.2 ± 1.0
	P3	24.8 ± 1.4	25.4 ± 1.5	12.0 ± 0.5	31.2 ± 2.4
$n_{H,lvg,p-H_2CO}$[d] ($\times10^4$ cm^{-3})	P1	5.4 ± 3.5	13.4 ± 7.6	11.4 ± 2.2	5.5 ± 1.2
	P2	4.7 ± 3.3	6.6 ± 1.4	9.3 ± 2.1	11.6 ± 2.1
	P3	7.8 ± 5.1	6.3 ± 4.2	12.5 ± 0.3	7.0 ± 1.4
T_{kin} (CO)[g] (K)	P1	10.9 ± 2.6	7.1 ± 1.5	12.0 ± 5.9	10.2 ± 1.5
	P2	25.1 ± 4.8	7.4 ± 1.2	11.1 ± 9.4	9.5 ± 0.9
	P3	36.2 ± 7.6	8.6 ± 0.6	22.9 ± 12.9	9.0 ± 3.0
$n_{H,lvg,CO}$[d] ($\times10^4$ cm^{-3})	P1	3.7 ± 2.6	3.0 ± 2.5	3.3 ± 2.8	3.1 ± 2.6
	P2	3.7 ± 2.8	3.0 ± 2.5	3.1 ± 2.7	3.1 ± 2.7
	P3	3.3 ± 2.8	3.3 ± 2.8	3.1 ± 2.7	3.1 ± 2.6

Notes.
[a] P1, P2, and P3 denote the DCO$^+$-dominant, transition, and CO-dominant zones, respectively. The given coordinates of P1 and P2 correspond to the 870 μm emission peaks, and those of P3 correspond to the 870 μm (G14.49–0.13 and G11.38+0.81) or 70 μm (G34.74–0.12 and G15.22–0.43) emission peaks.
[b] From the SED fit, achieving an angular resolution of 18″ or 20″.
[c] Here "$\cdots$" indicates a location where we do not have NH$_3$ observations.
[d] The H$_2$ and H number density is derived by an LVG fit of the p–H$_2$CO lines.
[e] T_{kin} derived from p–NH$_3$ (2,2)/(1,1) lines at an angular resolution of 34″.7.
[f] T_{kin} derived from an LVG fit of four p–H$_2$CO lines at an angular resolution of 35″.6.
[g] T_{kin} derived from an LVG fit of C^{18}O (2–1)/(1–0), C^{17}O (2–1)/(1–0), and ^{13}CO (2–1)/(1–0) lines at an angular resolution of 16″.4.

individual locations in G11.38+0.81 and G34.74–0.12 is in the range of 7–10 K, which is lower than T_{dust} at the same locations. The 2–1 lines, with critical densities (Table A2) not significantly less than n_H ($\sim3 \times 10^4$ cm^{-3}), may be subthermally excited. Therefore, we do not consider low-J CO isotopologue lines as reliable gas temperature tracers in this work. Nevertheless, the LVG estimates indicate that the C^{18}O(2–1) and C^{17}O(2–1) lines are optically thin ($\tau < 1$) toward the pixels where they are detected with S/N > 5. Moreover, we also derive the C^{18}O column densities by using T_{dust} and assuming that the 2–1 line is optically thin and in LTE. Compared to those, C^{18}O column densities derived from RADEX are higher by a factor of 2–3 toward a few locations, such as P1 and P2 in G11.38+0.81 and G14.49–0.13 (see Table A4). Nevertheless, the differences in the above estimates lie within the uncertainties.

Moreover, our IRAM 30 m observations covered four lines of p–H$_2$CO ($1_{0,1}-0_{0,0}$, $3_{0,3}-2_{0,2}$, $3_{2,2}-2_{2,1}$, $3_{2,1}-2_{2,0}$) that have been previously used as a gas thermometer (e.g., Mangum & Wootten 1993; Johnstone et al. 2003; Leurini et al. 2004, 2007; Ao et al. 2013; Ginsburg et al. 2016; Giannetti et al. 2017b; Tang et al. 2018; Feng et al. 2019). The $1_{0,1}-0_{0,0}$ ($E_u/k_B \sim 3$ K) and $3_{0,3}-2_{0,2}$ ($E_u/k_B \sim 21$ K) lines are detected with S/N > 4 toward all zones, while the $3_{2,2}-2_{2,1}$ and $3_{2,1}-2_{2,0}$ lines ($E_u/k_B \sim 68$ K) detected with low S/N (<3) can be used to constrain the upper limit of the gas temperature. Smoothing them to the same angular resolution (35″.6), we used RADEX and found that the gas kinetic temperatures derived from these lines, T_{kin} (p–H$_2$CO), are in the range of 12–37 K, higher than T_{kin} (p–NH$_3$) at the same spatial scale and T_{kin} (CO) at a smaller spatial scale. Possible reasons are as follows. (1) The H$_2$CO is likely formed in the gas phase as reaction products of hydrocarbons (Yamamoto 2017). The hydrocarbons are typically found in the outer regions of molecular clouds, where the gas temperature is higher than in the dense regions of the cold clumps (see the T_{dust} maps in Figure 1). (2) In the dense and cold clumps, H$_2$CO is probably frozen onto dust grains in the same way as CO and maybe transformed into CH$_3$OH in a relatively fast process. (3) The H$_2$CO lines have higher critical densities than the NH$_3$ lines

and CO isotopologue lines even at the same temperature (Table A2), so they may trace different gas.

3.2.3. Depletion Factor Map of $C^{18}O$

Assuming that $C^{18}O(2-1)$ is optically thin and under LTE toward each pixel (Section 3.2.2), we derived the column density of $C^{18}O$ toward P1, P2, and P3 by using the dust temperature T_{dust} and gas kinetic temperature T_{kin} (p–NH$_3$) at an angular resolution of $\sim35''$. For testing the effect of the gas temperature uncertainty on the measurement of the column density uncertainty, we also use T_{kin} (p–H$_2$CO) at the same angular resolution. We found that the estimates of $C^{18}O$ column density by using different temperature sets at individual pixels are consistent within the uncertainty (Table A4). Furthermore, when the gas temperature is in the range of 11–40 K, an uncertainty of 10 K (at most) brings in 15% uncertainty on the accuracy of the $C^{18}O$ column density estimates. In the interest of higher angular resolution and less uncertainty, we use the T_{dust} map to derive the observed $C^{18}O$ column density (denoted as $N^o_{C^{18}O}$) map.

Statistically, in a star-forming environment without CO depletion, its relative abundance $\chi^E(^{12}CO)$ with respect to H$_2$ is expected to change with galactocentric distance R_{GC}. Moreover, the $\mathcal{R}_{^{16}O/^{18}O}$ isotopic ratio changes with galactocentric distance as well, so the $C^{18}O$ column density is expected (denoted as $N^E_{C^{18}O}$) to be correlated with the observed H$_2$ column density as (Frerking et al. 1982; Wilson & Rood 1994; Giannetti et al. 2014)

$$N^E_{C^{18}O} = \frac{N^E_{^{12}CO}}{\mathcal{R}_{^{16}O/^{18}O}} = \frac{\chi^E(^{12}CO)}{\mathcal{R}^E_{^{16}O/^{18}O}}N_{H_2}$$
$$= \frac{9.50 \times 10^{-5}e^{(1.11-0.13R_{GC}(kpc))}}{58.80R_{GC}(kpc) + 37.10}N_{H_2}. \quad (1)$$

Then, the $C^{18}O$ depletion factor (Figure 2) can be derived as

$$f_D(C^{18}O) = \frac{N^E_{C^{18}O}}{N^o_{C^{18}O}}. \quad (2)$$

The sources in our pilot sample are at the galactocentric distance $R_{GC} = 5.4 \pm 0.5$ kpc. Apart from G11.38+0.81, where $f_D(C^{18}O)$ is higher than the rest of the sources by a factor of 2–3, the maximum of the $f_D(C^{18}O)$ appears toward the P1 (or P2) of each region, reaching 4.2 ± 0.5 at a linear scale of 0.18–0.46 pc (an angular resolution of $20''$). Moreover, smoothing the dust and $C^{18}O$ line emission from $20''$ to $35''$ does not change the $f_D(C^{18}O)$ estimates. Without analyzing the entire sample of 24 regions, we are not able to test whether or not the absolute value of $f_D(C^{18}O)$ shows a correlation with the source R_{GC}. Nevertheless, when comparing the relative $C^{18}O$ depletion factor toward locations in individual sources, we note that the largest $f_D(C^{18}O)$ values toward P1 or P2 are higher than those toward P3 (the CO-dominant zone) by a factor of 1.4–3, with small uncertainties (Table 3).

3.2.4. D-fraction Map of HCO^+

Assuming that the $\mathcal{R}_{^{12}C/^{13}C}$ isotopic ratio changes with R_{GC} (Giannetti et al. 2014), having no variation within each source, and that the 1–0 lines from H^{13}CO$^+$ and DCO$^+$ are optically thin (e.g., Sanhueza et al. 2012; Feng et al. 2016b), the D-fraction map of HCO$^+$ toward each source can be derived

Table 3
Relative Ratios of $C^{18}O$ Depletion Factor and HCO$^+$ D-fraction between Locations

Zones[a]	$f_D(C^{18}O)$[b,c]		D_{HCO^+}[b,d,e]	
	P1/P3[f]	P2/P3[f]	P1/P3[f]	P2/P3[f]
G15.22–0.43	2.7 ± 0.0	1.8 ± 0.0	>2.9	>1.0
G11.38+0.81	1.4 ± 0.1	0.8 ± 0.0	>2.2	>1.3
G14.49–0.13	1.9 ± 0.1	1.3 ± 0.1	1.2 ± 0.1	<0.3
G34.74–0.12	1.8 ± 0.0	2.1 ± 0.0	>1.4	⋯

Notes.
[a] P1, P2, and P3 denote the DCO$^+$-dominant, transition, and CO-dominant zones, respectively.
[b] Value derived by using T_{dust} at an angular resolution of $34''.7$.
[c] The $C^{18}O$ depletion is derived by assuming the expected abundance with respect to H$_2$ as Equations (1)–(2) and assuming a gas-to-dust mass ratio $\log(\gamma) = 0.087R_{GC}$ (kpc) + 1.44 (Draine 2011; Giannetti et al. 2017b).
[d] The D-fraction is derived from the DCO$^+$(1–0) and H^{13}CO$^+$(1–0) lines by assuming that they are optically thin, have the same beam filling toward each pixel, and have a fraction of $\mathcal{R}_{^{12}C/^{13}C} \sim 6.1R_{GC}$(kpc) + 14.3 (Giannetti et al. 2014).
[e] A lower or upper limit is given when the detected DCO$^+$(1–0) shows $<3\sigma$ emission toward P3 or P2.
[f] Values are given as the relative ratio between two locations.

from the relative abundance ratio map of DCO$^+$ with respect to H^{13}CO$^+$ as (Figure 2)

$$D_{HCO^+} = \frac{\chi(DCO^+/H^{13}CO^+)}{\mathcal{R}_{^{12}C/^{13}C}} = \frac{\chi(DCO^+/H^{13}CO^+)}{6.1R_{GC}(kpc) + 14.3}. \quad (3)$$

Using the three temperature sets T_{dust}, T_{kin} (p–NH$_3$), and T_{kin} (p–H$_2$CO) at an angular resolution of $\sim35''$, we found that D_{HCO^+} toward the same location does not show much difference ($<10\%$; see Table A4). Instead, each D_{HCO^+} map shows a trend, dropping from P1, the DCO$^+$-dominant region (1%–2%), to P3 (where $C^{18}O$ shows the maximum abundance in G15.22–0.43 and G11.38+0.81) and P2 (where both $C^{18}O$ and DCO$^+$ are deficient in G34.74–0.12 and G14.49–0.13) by a factor of more than 2 (Table 3).

3.2.5. Error Budget

Above, we discussed the validity of our assumptions to treat the H^{13}CO$^+$(1–0), DCO$^+$(1–0), and $C^{18}O$(2–1) lines as optically thin and in LTE condition (Sections 3.2.2–3.2.4). However, we are not able to test the validity of the other assumptions in our measurements, such as the unity beam-filling factor for the low-J lines with extended emission, the constant conversion factor of gas-to-dust mass ratio γ, the expected gas-phase abundance of CO with respect to H$_2$ (without depletion), the same depletion factor for CO and $C^{18}O$, and the fractionation of $\mathcal{R}_{^{12}C/^{13}C}$ and $\mathcal{R}_{^{16}O/^{18}O}$. Nevertheless, in the context of only the relative trend in the $f_D(C^{18}O)$ and D_{HCO^+} maps toward the same cloud, these uncertainties are canceled out (see Table 3).

4. Discussion

In the sources of our pilot sample, the $f_D(C^{18}O)$ is high (>3) toward the DCO$^+$-dominant zone with high optical extinction (Av > 20 mag; see Güver & Özel 2009). The N_{H_2} toward this zone is denser than that toward the CO-dominant zone (Av $\sim$ 10–15 mag) by a factor of 2. Similar to the findings in previous studies (e.g., Pagani et al. 2005), the difference in self-shielding

of CO may not be responsible for the trend in the $f_D(C^{18}O)$ toward the same natal cloud. Therefore, it is worth investigating whether the variation in gas number density and/or the source temperature leads to such an $f_D(C^{18}O)$ trend, and whether the chemical relation between the CO depletion and D-fraction of HCO^+ can give a constraint on the chemical age of our sources.

4.1. Comparison with Previous Works

Our sources are selected at different kinematic distances, i.e., progressively further away from the Sun by 1 kpc. Comparing the absolute value of $f_D(C^{18}O)$ toward the pilot sample at the same angular resolution (16″ or smoothing to 35″, corresponding to 0.2–1 pc), we find that the maxima of $f_D(C^{18}O)$ toward the pilot sample regions are similar. In general, they appear as 4–6 at the locations with T_{dust} in the range of 14–18 K (Figure 2). The exception is G11.38+0.81, where the maximum of $f_D(C^{18}O)$ is higher (up to 15) than the rest of the sources toward the region with colder T_{dust} (12 K).

Compared to previous studies, the absolute values of $f_D(C^{18}O)$ in our regions are generally consistent with those toward low-mass clouds (e.g., Bacmann et al. 2003; Ceccarelli et al. 2007; Christie et al. 2012) and high-mass clumps (e.g., Hernandez et al. 2011; Liu et al. 2013; Rygl et al. 2013; Sabatini et al. 2019). Moreover, the high value toward G11.38 +0.81 is consistent with those found at a comparable linear resolution from large sample studies of high-mass clumps in Fontani et al. (2012; in a range of 50–80, being two to three times larger because of the use of a different dust opacity) and Giannetti et al. (2014; up to 20 toward the cold and young clumps), where γ was adopted as 100. A similar case of higher $f_D(C^{18}O)$ is also found toward G35.39–0.33 at a linear resolution of 0.2 pc, where $f_D(C^{18}O)$ is up to 4 in a region with $n_H \sim 10^3$ cm^{-3} (Hernandez et al. 2011) and up to 12 in regions with $n_H \sim 10^4$ cm^{-3} (Jiménez-Serra et al. 2014).

We also note that $f_D(C^{18}O)$ measured in our regions at a linear scale of >0.1 pc is smaller than that measured at a 0.01 pc scale. This is consistent with $f_D(C^{18}O)$ found toward our pilot source, G28.34+0.06 ($R_{GC} \sim 4.6$ kpc), ~5 at a linear resolution of 0.8 pc (Feng et al. 2019),[25] while it is 10^2–10^3 at a linear resolution of 0.01 pc (Zhang et al. 2009; Urquhart et al. 2018). The gas number density at different scales, as well as beam dilution for relatively compact $C^{18}O$ emission, could be reasons for the different magnitudes in measuring $f_D(C^{18}O)$.

Although we give the absolute values of $f_D(C^{18}O)$ in Figure 2, in the following, we focus on the relative trends observed from the 70 μm dark region (P1) to the 70 μm bright region (P3) for the uncertainty of the gas and dust conversion constants used in our analysis (see Section 3.2.5). The depletion factor $f_D(C^{18}O)$ decreases toward individual sources from P1 to P3 by a factor of 2–4, behaving the same as those found from the less evolved to the more evolved high- and low-mass clumps (e.g., Christie et al. 2012; Fontani et al. 2012; Giannetti et al. 2014).

The projected distance from the depletion maximum (P1) to the minimum (P3) in our regions is in the range of 0.5–2 pc. This is comparable to, or at most twice, the width of each filament (0.5–1 pc), obtained from the size of the 870 μm continuum contour with S/N < 5. This feature is also found in

a nearby high-mass region, G351.77-0.51 ($R_{GC} < 1$ kpc), where Sabatini et al. (2019) suggested that a depletion radius (0.02–0.15 pc) is comparable to the filament width (0.1 pc).

### 4.2. Possible Spatial Correlation between the Dust and Gas Properties

In our observations, the dust and gas appear to be thermally coupled (T_{dust} is close to T_{kin} (p–NH$_3$) toward individual pixels), and T_{dust} does not significantly change with angular resolution from 20″ to 36″. Five parameters derived from dust and gas emissions—T_{dust}, the H$_2$ column density (N_{H_2}), the gaseous column densities of DCO$^+$ (N_{DCO^+}), C^{18}O ($N^o_{C^{18}O}$), and H^{13}CO$^+$ ($N_{H^{13}CO^+}$)—show variations as a function of location within each region. Smoothing these variable maps to the same angular resolution (36″), we extract their absolute values from each pixel and plot the bivariate Gaussian kernel density maps of several variable pairs (Figures 3 and A2). The red, blue, and yellowish-green areas represent the variables extracted from the CO-dominant, DCO$^+$-dominant, and transition zones, respectively. Moreover, to understand whether each pair of variables is correlated or not, we measure their Spearman's rank correlation[26] coefficient ρ (Cohen 1988) toward different zones, as well as toward the entire mapping region. In the following discussion, we define the relationship between two variables as a "strong correlation" when $|\rho| \geqslant 0.5$, a "moderate correlation" when $0.5 > |\rho| \geqslant 0.3$, a "weak correlation" when $0.3 > |\rho| \geqslant 0.1$, and "no correlation" when $|\rho| < 0.1$.

From Figures 3 and A2, we find the following.

1. The N_{H_2} and T_{dust} are strongly anticorrelated ($\rho < -0.5$). In general, the DCO$^+$-dominant zone (P1) in each region is 3–6 K colder and two to three times higher than the neighboring CO-dominant zone (P3). Although a more robust fit is required to be applied to the full sample of regions, the linear proportion index between the logarithm of N_{H_2} and the T_{dust} of all four sources appears similar (will be discussed in Section 4.3), so this pair of variables seems to be dependent.

2. The abundance of gaseous C^{18}O is strongly correlated with T_{dust} ($\rho > 0.5$), and the D_{HCO^+} shows a strong or moderate anticorrelation with T_{dust} ($\rho < -0.4$; Figure A2). For all four regions, the colder gas toward P1 has consistently lower values of the relative gaseous abundance ratio $\chi(C^{18}O/DCO^+)$ than the warmer gas toward P3, showing a robust trend of increasing $\chi(C^{18}O/DCO^+)$ with the evolutionary stage of the star-forming clump. This is consistent with chemical model predictions (see Section 4.3), where higher temperatures enhance the C^{18}O abundance (lower depletion) and suppress the deuteration of other species (e.g., Roberts & Millar 2000; Caselli et al. 2008).

3. The abundances of gaseous H^{13}CO$^+$ and C^{18}O are strongly correlated ($\rho > 0.5$), except for G14.49–0.13. Apart from G14.49–0.13, denser gas traced by a higher abundance of H^{13}CO$^+$ (6×10^{-11}) toward each region shows a relatively higher abundance of gas-phase C^{18}O (1.5×10^{-7}) than the rest by a factor of more than 3. As

---

[25] The $f_D(C^{18}O)$ is measured up to 10 by adopting $\gamma \sim 150$ in Feng et al. (2019) and corrected up to 5 by adopting $\gamma \sim 70$ at $R_{GC} \sim 4.6$ kpc.

[26] Spearman's rank correlation coefficient ρ is a nonparametric measure of statistical dependence between two variables (Cohen 1988). This coefficient can assess how well a monotonic function (no matter whether linear or not) can describe the relationship between two variables. The coefficient ρ is in the range from −1 (decreasing monotonic relation) to 1 (increasing monotonic relation), with zero indicating no correlation.
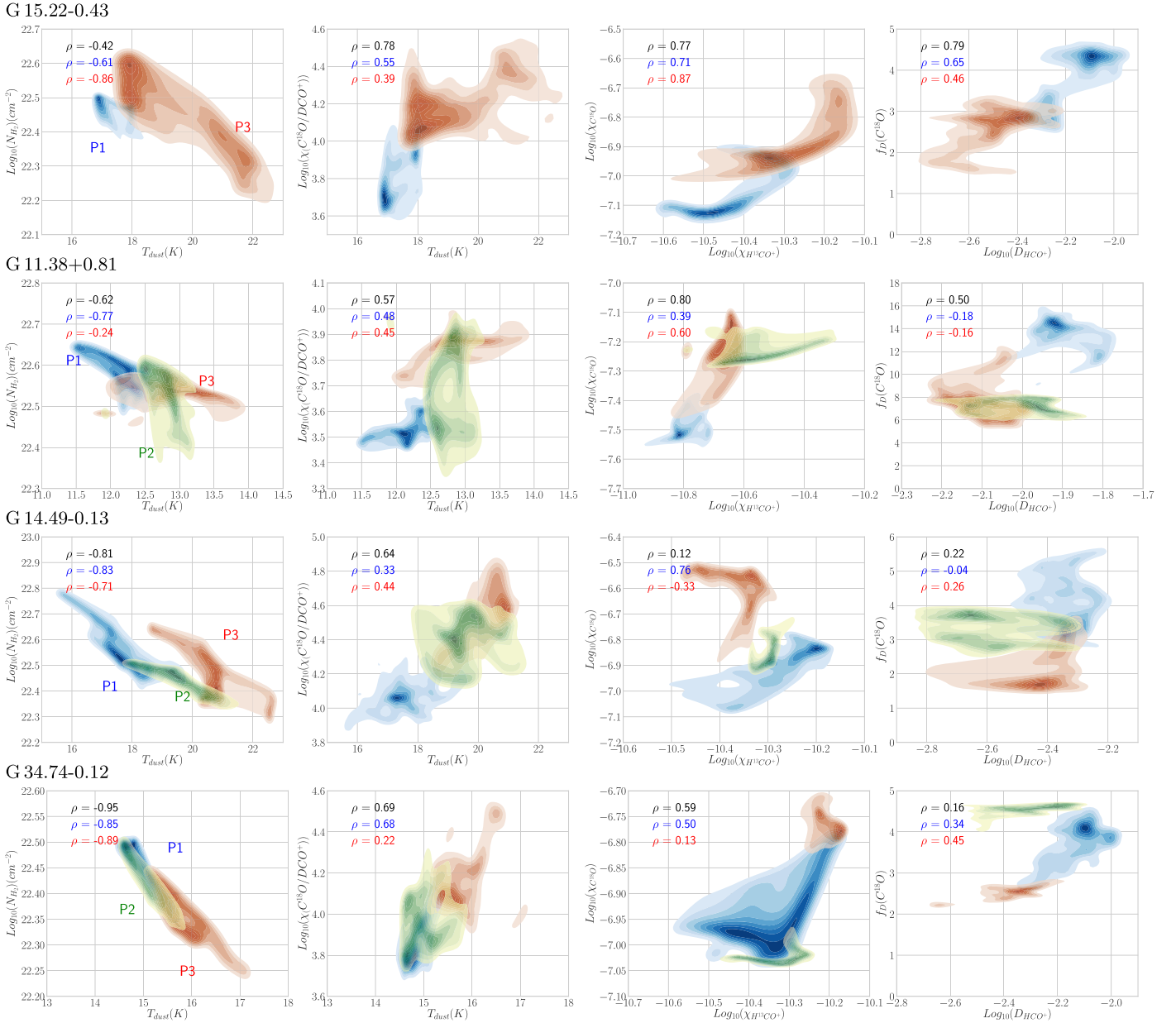
Figure 3. Possible correlation between variables. Values are extracted from pixels after smoothing the parameter maps to the same angular resolution (36″) and plotted with a bivariate Gaussian kernel density estimate as contours. The CO- and DCO$^+$-dominant zones are plotted in red and blue, with the Spearman's rank correlation coefficient ρ given in red and blue, respectively. The transition zone is plotted in yellowish-green. The Spearman's rank correlation correlation coefficient ρ of the entire region is given in black. The pixels where continuum at 870 μm shows <5σ emission or DCO$^+$(1–0) shows <3σ emission are blanked.

for G14.49–0.13, gaseous C^{18}O and H^{13}CO$^+$ show a strong correlation only toward the DCO$^+$-dominant zone, while the maximum abundance of gaseous C^{18}O is not spatially coincident with the H^{13}CO$^+$. On the one hand, this could be an apparent effect, due to the fact that the H^{13}CO$^+$(1–0) line with high critical density is more efficiently excited (i.e., showing stronger emission) in the dense regions where CO is frozen out. On the other hand, several protostellar cores with outflows were detected toward G14.49–0.13 at a linear resolution of 0.01 pc (Li et al. 2019; Sanhueza et al. 2019). Therefore, zones with an enhanced ionization fraction in the vicinity of protostellar sources may show a larger abundance of H^{13}CO$^+$ (see, e.g., Ceccarelli et al. 2014).

4. The f_D(C^{18}O) and D_{HCO^+} show a strong correlation toward the entire region of G15.22–0.43 and G11.38 +0.81 and a moderate correlation toward G14.49–0.13 and G34.74–0.12 when excluding the transition zone. The primary chemical process in the low-temperature (<20 K) DCO$^+$-dominant zone, after the onset of CO freeze-out, is the conversion of the remaining gaseous CO into DCO$^+$ in reactions involving H$_2$D$^+$ and D$_2$H$^+$ (e.g., Watson 1976; Gerlich & Schlemmer 2002; Caselli et al. 2008; Aikawa et al. 2018). Therefore, with more CO depleted, more H$_3^+$ takes part in deuterium enrichment and increases the D-fraction of species, including HCO+. This trend is also seen in, e.g., Caselli et al. (2002b), Tielens (2013), and Redaelli et al. (2019). In a warm
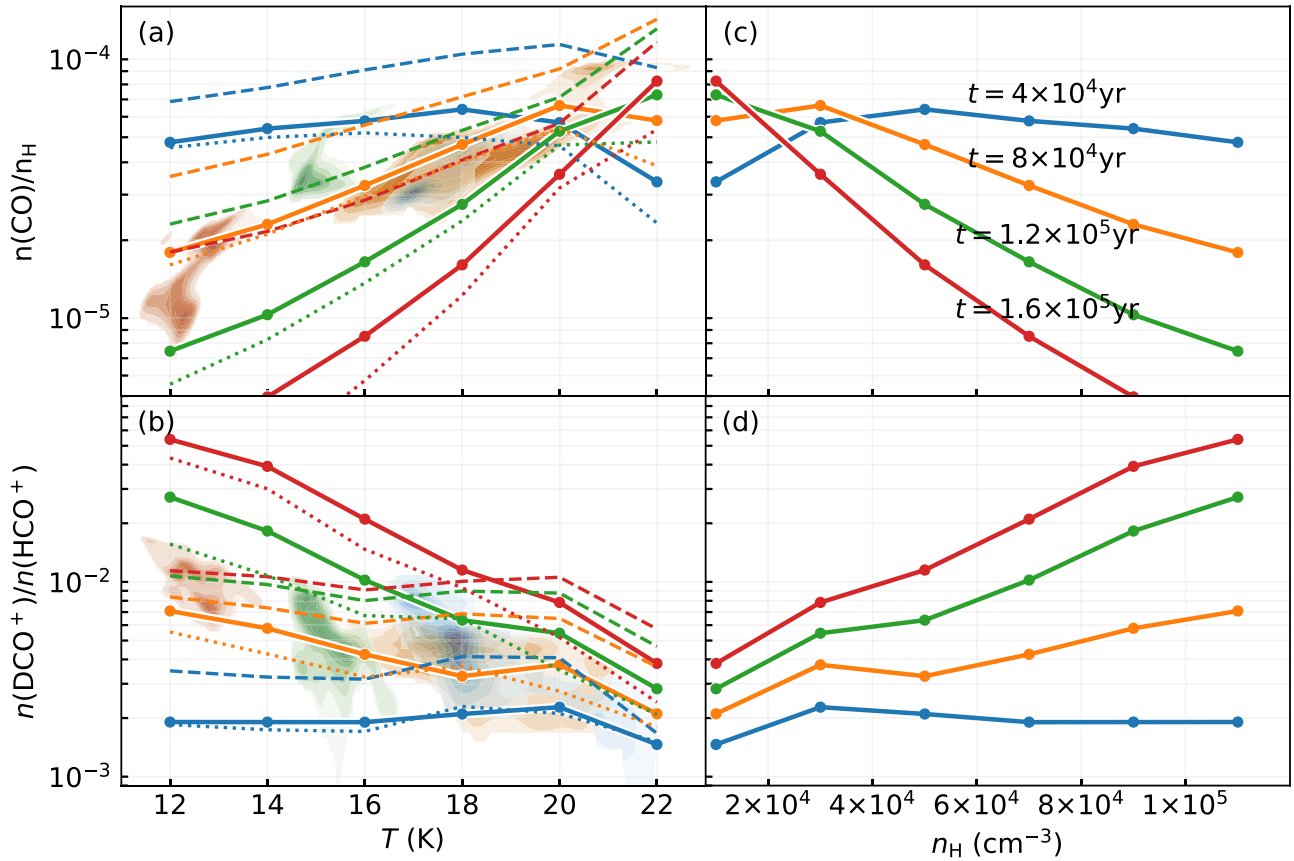
Figure 4. Modeled CO abundance (relative to hydrogen) and D-fraction of HCO^+ as a function of temperature and gas number density, evaluated at different time points (shown with different colored lines). The left and right panels appear to be mirror reflections of each other because temperature and density are linearly anticorrelated in the models. The observational data of each source are plotted as a bivariate Gaussian kernel density map in the background (red: G11.38+0.81; orange: G14.49–0.13; blue: G15.22–0.43; and green: G34.74–0.12; see also Figure A2). The solid orange curve is considered to be a "fit" to the four regions. The solid curves are calculated with a canonical CRIR of $1.36 \times 10^{-17} \, s^{-1}$, while the dashed and dotted curves correspond to 10 times higher or lower than this value.

protostellar environment, CO desorbs to the gas phase, producing the CO-dominant zone. Moreover, DCO^+ is not efficiently formed; instead, it is destroyed mainly through electron recombination.

4.3. Chemical Modeling

To understand the trends (at least qualitatively) seen in the observational data, we first put together the observational data points of the four sources with the coordinates as $(T, \chi[CO])$ and $(T, D[HCO^+])$ (the colored bivariate Gaussian kernel density contours in Figure 4). Since the density contours from all sources are overlapped or well connected with the same slope in both plots, we assume that they have a similar nature. Then we aim to reproduce the correlations seen in the plots by running a set of models using a chemical code called chempl (Du 2020). This chemical code is based on the "three-phase" description of interstellar chemistry, namely, species in the model can be in the gas phase, on the dust grain surface, and in the dust grain mantle. The chemical network is based on the UMIST 2012 database (McElroy et al. 2013), "deuterated" by adding deuterium to the network (Roberts et al. 2003, 2004), and augmented by adding grain surface reactions from Hasegawa et al. (1992) and recent experimental results. In total, 35,457 reactions are included in the calculation.

Our models are "pseudo-time-dependent," in the sense that the physical conditions are kept constant; namely, parameters

such as temperature and density do not change with time (see, e.g., Hassel et al. 2010). The abundances of different species do evolve with time, starting from an assumed initial distribution; i.e., all of the elements are atomic, except for H and D, which are assumed to be in H_2 and HD molecules. This types of initial conditions are traditionally used in astrochemical modeling (e.g., Hasegawa et al. 1992; Lee et al. 1996; Roberts et al. 2004; Garrod et al. 2008; Pagani et al. 2011).

We did not conduct a complete parameter search to find the "best fit," partly because the uncertainties associated with the data may make a best fit not very meaningful and partly because, due to the uncertainties of the many different parameters used by the model, a parameter search will be computationally very expensive. Hence, we choose to model the data heuristically by adopting a set of physically reasonable parameters.

When adopting a constant density, with the temperature in the range of ~14–20 K (assuming $T_{dust} = T_{gas}$), we were not able to reproduce the observed correlation between the temperature and CO abundance (Figure A2). Namely, in such models, the gas-phase CO abundance *decreases* with temperature. This may seem counterintuitive at first sight. The underlying reason is that, as the dust grain temperature increases, reactions on the dust grain surface become more efficient to form species such as CO_2 (e.g., Garrod 2013), which cannot easily evaporate into the gas phase at such low temperatures. Thus, in the current set of models, we let the

density vary as a function of temperature. Specifically, we let

$$n_{\rm H}({\rm cm}^{-3}) = (23 - T_{\rm dust}({\rm K})) \times 10^4 \qquad (4)$$

to semiquantitatively reflect the anticorrelation between density and temperature seen in the observational data (Figure 3).

The modeling results are shown in Figure 4, in which the curves show the CO abundance and $D_{\rm HCO^+}$ as a function of temperature and gas number density at different times. Though quite simple, the models already provide some interesting insights. (1) As part of the heuristics, to match the observed CO abundance and its correlation with temperature, we have used enhanced elemental abundances of carbon and oxygen (2×10^{-4} and 5×10^{-4} instead of the frequently adopted 1.4×10^{-4} and 3.2×10^{-4}; Garrod et al. 2008).

(2) To match the observed $D_{\rm HCO^+}$ trend, the D/H abundance ratio is set to 3×10^{-6}, a factor of ~5 lower with respect to the usual value of $(1.5$–$2) \times 10^{-5}$. This is consistent with previous works on the Galactic elemental abundance gradient of deuterium, carbon, and oxygen (Smartt & Rolleston 1997; Lubowich et al. 2000; Carigi et al. 2005; Lubowich & Pasachoff 2010; Esteban & García-Rojas 2018), considering that the sources in the current work have galactocentric distances $R_{\rm GC} \sim 5$ kpc.

(3) An approximate "fitting" to the observed trends can be obtained from Figure 4 for a chemical age of $\sim 8 \times 10^4$ yr (solid orange curve). Although there is no agreed-upon definition for the point of age zero in modeling, here we implicitly define it as the stage in which all of the elements are atomic except for H and D (in the form of H_2 and HD). For the fitting to χ(CO) (panel (a) of Figure 4), the CO abundance is mainly determined by adsorption and desorption. A longer age would lead to CO abundances lower than observed. As noted before, the increase of CO abundance with temperature in that panel is *not* caused by the increased evaporation rate but rather by the T–$n_{\rm H}$ relation (Equation (4)) implemented in our model. For the fitting to $D_{\rm HCO^+}$ (panel (b) of Figure 4), a longer age would cause a $D_{\rm HCO^+}$ higher than observed. The age cannot be shorter than $\sim 10^5$ yr as well, otherwise the abundance of DCO$^+$ would not be high enough ($\gtrsim 10^{-11}$) to be detectable.

Since we covered only a small fraction of the parameter space, there are caveats associated with the fitting and the derived nominal chemical age. First of all, putting together the observational data of CO abundance and D-fraction of HCO$^+$, we have made a rather strong hypothesis that these sources are of similar nature because the data show the same trend in the plots of $(T, \chi[{\rm CO}])$ and $(T, D_{\rm HCO^+})$ (Figure 4). Moreover, our definition of the age zero-point is from the point of view of the formation of a molecular cloud. However, an appropriate assumption for the initial conditions depends on a "proper" choice of chemical age tracer. A better approach would be to look at the overall chemical inventory and see whether or not one can identify a variety of "early-type" molecules in the cloud(s).

Second, our model does not take into account the spin states of H_2 and other related species. It is known that the abundances of deuterated species can be significantly affected by the ortho-para ratio (o/p ratio) of H_2 (Sipilä et al. 2010; Pagani et al. 2011; Furuya et al. 2015; Sipilä et al. 2017), because o-H_2 has a higher-energy ground state than p-H_2, and it can more efficiently destroy the deuterated isotopologues of H_3^+ (H_2D^+, D_2H^+, D_3^+), thus reducing the abundances of deuterated species derived from them. It has been experimentally demonstrated by

Watanabe et al. (2010) that H_2 molecules freshly formed on amorphous solid water have a statistical o/p ratio of 3, and that this o/p ratio can change when H_2 molecules are retrapped by the water ice. Moreover, the o/p ratio of H_2 can also be altered by gas-phase processes. The initial o/p ratio of H_2 that was adopted by chemical models is subject to large uncertainties (e.g., Pagani et al. 2011; Bovino et al. 2017). One issue is that we do not know how long it takes for atomic hydrogen to become molecular, which affects the evolution of the o/p ratio, especially under the circumstance when a molecular cloud may have gone through many dispersal–reassembly cycles (H_2 molecules may mostly be kept intact, while other species may be destroyed and reformed; e.g., Chevance et al. 2020). If we take into account the spin states of H_2 in our model, the deuteration process would be delayed, i.e., the chemical age would be longer, and this would render CO abundances lower than observed.

Third, we used a "canonical" CRIR of 1.36×10^{-17} s^{-1}. Cosmic-ray ionization is the main driving force of chemistry in shielded regions. A moderately high CRIR can shorten the chemical evolution timescale and, specifically, help the conversion from o-H_2 to p-H_2. It is known that the CRIR is higher in the inner region of the Galactic disk (Indriolo et al. 2015; Neufeld & Wolfire 2017). Since the four sources are at galactocentric distances of ~5 kpc, their CRIR could be higher than the canonical value. Scaling the canonical CRIR value up or down by a factor of 10 (dashed and dotted curves in Figure 4) does not improve the fitting to the CO abundance and $D_{\rm HCO^+}$ trends. More comprehensive parameter studies, such as an MHD model coupled with chemical properties from the entire sample of sources, are needed to get more quantitative constraints.

4.4. Dynamical and Chemical Timescales

Three timescales can be used to characterize the evolutionary status of our sources.

In an ideal case of supercritical collapse, the free-fall timescale of a cloud is defined as

$$t_{\rm ff} = \left(\frac{3\pi}{32 G \rho_{\rm gas}} \right)^{1/2} \simeq 1.38 \times 10^6 \, ({\rm yr}) \left(\frac{n_{\rm H}}{10^3 \, {\rm cm}^{-3}} \right)^{-1/2}. \quad (5)$$

In reality, physical mechanisms such as magnetic field and turbulence provide support against gravitational collapse. Therefore, the contraction speed of the clouds is in general observed as a fraction ($\eta \sim 20\%$–50%) of the free-fall speed (e.g., Evans 2003; Wyrowski et al. 2012, 2016; also found in our entire sample of sources, S. Feng et al. 2020, in preparation). The contraction timescale can be computed from the observation as

$$t_{\rm contr} \sim t_{\rm ff} / \eta. \qquad (6)$$

The timescale for CO molecules to freeze out onto dust grains is

$$t_{\rm ads,CO} = \left(S \pi a^2 \sqrt{\frac{8 k_{\rm B} T_{\rm kin}}{\pi m_{\rm CO}}} \, n_{\rm grain} \right)^{-1}$$

$$\simeq 1.2 \times 10^6 \, ({\rm yr}) \, S^{-1} \left(\frac{T_{\rm kin}}{10 \, {\rm K}} \right)^{-1/2}$$

$$\times \left(\frac{n_{\rm grain}}{10^{-8} \, {\rm cm}^{-3}} \right)^{-1} \left(\frac{a}{0.1 \, \mu{\rm m}} \right)^{-2}, \qquad (7)$$

where S is the sticking coefficient, a is the dust grain radius, and the meaning of the other symbols should be self-evident (Caselli et al. 1999; Aikawa 2013).

Expressed in terms of gas density n_H, the adsorption timescale can be written as

$$t_{ads,CO} = \left(\frac{3S}{4a} \sqrt{\frac{8k_B T_{kin}}{\pi m_{CO}}} \frac{n_H m_H \mu}{\gamma \rho_{grain}} \right)^{-1}$$

$$= 4.2 \times 10^5 \, (yr) \left(\frac{T_{kin}}{10 \, K} \right)^{-1/2} \left(\frac{n_H}{10^4 \, cm^{-3}} \right)^{-1} \left(\frac{\mu}{1.4} \right)^{-1}$$

$$\times \left(\frac{a}{0.1 \, \mu m} \right) \left(\frac{\gamma}{100} \right) \left(\frac{\rho_{grain}}{2 \, g \, cm^{-3}} \right). \tag{8}$$

Hence, we have

$$\frac{t_{ff}}{t_{ads,CO}} \simeq 0.75 \times \left(\frac{T_{kin}}{10 \, K} \right)^{1/2} \left(\frac{n_H}{10^4 \, cm^{-3}} \right)^{1/2} \left(\frac{\mu}{1.4} \right)$$

$$\times \left(\frac{a}{0.1 \, \mu m} \right)^{-1} \left(\frac{\gamma}{100} \right)^{-1} \left(\frac{\rho_{grain}}{2 \, g \, cm^{-3}} \right)^{-1}. \tag{9}$$

To match with both the observed CO abundance and D_{HCO^+} in our source environment, with $n_H \sim 10^4$–10^5 cm^{-3} in our 70 μm dark sources (Table 2),[27] our preliminary chemical modeling prefers a chemical age of the sources, in terms of $t_{ads,CO}$, of $\sim 8 \times 10^4$ yr (Section 4.3 and Figure 4). This chemical age appears to be comparable to or slightly shorter than the free-fall timescale t_{ff} ($(1-4) \times 10^5$ yr), and also shorter than the t_{contr} ($\sim 10^6$ yr). The above timescale estimates are based on the assumption that n_H does not change with time. In reality, n_H is increasing from a less dense initial condition, e.g., $\sim 10^3$ cm^{-3}, to the current status. Therefore, it takes longer time from the age zero-point until now ($t_{ads,CO}$) than the above estimates, and will take more years for the cloud to contract (t_{contr}) than the above prediction.

In these dense gas clumps, the CO depletes fast, so the clumps are expected to dynamically evolve to young protostellar objects. It is possible that the observed sources in this work are at a crossing point of fully developed CO depletion and the onset of global collapse. These are expected to be rare objects, given their short lifetime. This may also be a reason why only a few cases of parsec-scale CO depletion were reported toward high-mass star-forming regions so far, compared to the commonly reported subparsec-scale CO depletion toward much closer and more compact low-mass regions (e.g., Caselli et al. 1999; Kramer et al. 1999; Tafalla et al. 2002; Pineda et al. 2010).

Of course, many details in these processes need to be further scrutinized. In the future, such a comparative analysis will be applied to the entire sample. More comprehensive chemical modeling taking into account the spin states of H_2 and other relevant species (Hugo et al. 2009; Sipilä et al. 2010; Kong et al. 2015; Bovino et al. 2017) and coupling with dynamical evolution (e.g., Goodson et al. 2016; Bovino et al. 2019) is needed to understand the feedback of protostellar heating on

the depletion efficiency and therefore to profile the entire evolutionary process of these sources.

5. Conclusions

With the aim of characterizing the kinematic and chemical properties of the initial conditions for HMSF, we carried out a line-imaging survey project (MIAO) toward a sample of 24 relatively near ($d < 5$ kpc) IRDCs. This project uses single-dish (IRAM 30 m and NRO 45 m) and interferometric (ALMA) telescopes to image pairs of neighboring 70 μm bright and dark clumps at different spatial scales of individual regions, from parsec-scale filamentary clouds down to 0.01 pc–scale dense cores. The comparative analysis is applied to each region, which improves the robustness by canceling out calibration uncertainties.

In the present work, we focus on a detailed study of the parsec-scale CO depletion toward four regions (G11.38+0.81, G15.22–0.43, G14.49–0.13, and G34.74–0.12) from IRAM 30 m and NRO 45 m observations. Showing the spatial correlation between the CO depletion factor and the source physical structure (gas and dust temperature and density), we discuss the interplay between CO depletion and D-fractionation of HCO$^+$.

Our conclusions are as follows.

1. Our observations cover two transitions (1–0 and 2–1) from three CO isotopologues (^{13}CO, C^{18}O, and C^{17}O). They show anticorrelated spatial distributions with the dense gas tracers (1–0 lines of H^{13}CO$^+$ and DCO$^+$) in our sample sources, indicating that a high degree of CO depletion appears toward the cold, dense, 70 μm dark clumps.

2. The SED fits to multiwavelength continuum data indicate strong spatial anticorrelation between H_2 column density and the dust temperature of each source.

3. The LVG analysis indicates that the kinetic temperature derived from NH_3 is consistent with the dust temperature, and that the C^{18}O(2–1), H^{13}CO$^+$(1–0), and DCO$^+$(1–0) lines are reasonably assumed as optically thin and under LTE conditions in our source environment (with $T < 20$ K and $n_H \sim 10^4$–10^5 cm^{-3}).

4. The gas kinetic temperature measured with different thermometers (p–NH$_3$ lines, p–H$_2$CO lines, and CO isotopologue lines) varies by a factor of up to 2. Although such a difference increases the uncertainty of the molecular column density measurement toward a certain location, it does not result in a large uncertainty in f_D(C^{18}O) or D(HCO$^+$) in terms of the relative abundance ratio between molecules.

5. Separating each region into a DCO$^+$-dominant zone (P1), a CO-dominant zone (P3), and a transition zone (P2), we find that f_D(C^{18}O) and D(HCO$^+$) vary as a function of location, showing a robust decrease from P1 (with f_D(C^{18}O) as 5–20 and D(HCO$^+$) as 0.5%–2%) to P3 by a factor of more than 3 within a spatial extension of 2 pc. The main reason for such a trend is the different evolutionary stages of the neighboring clumps in the same cloud, which show a distinctive difference in temperatures at a linear scale of 0.1–0.5 pc.

6. To match the observed molecular abundances and trends, our preliminary chemical modeling prefers chemical ages for our sources of $\sim 8 \times 10^4$ yr, which is comparable to

---

[27] Assuming that the clouds have a spherical structure, with a length along the line of sight L close to its projected width, i.e., 0.5–1 pc in our sources, $n_H \sim N_{H_2}/L$. According to our SED fit, N_{H_2} in our sources is in the range of 10^{22}–10^{23} cm^{-2}, and n_H is in the range of 10^4–10^5 cm^{-3}.

their free-fall timescales and smaller than their contraction timescales. This indicates that our sources are at an early dynamical and chemical evolution. With future modeling incorporating the effects of the spin states of H_2 and dynamical evolution, we expect to get a more thorough understanding of the evolution of these sources.

7. Limited by the sensitivity of previous observational instruments, CO depletion was commonly reported at subparsec scale toward much closer and more compact low-mass star-forming regions. Fast-growing high-quality spectral imaging projects will allow us to reduce observational bias; thus, parsec-scale CO depletion is expected to be commonly observed toward more distant high-mass star-forming regions.

Appendix

Figure A1 shows the profile of the CO and HCO^+ isotopologue lines we use to measure the molecular column densities toward the four sources.

Figure A2 shows the possible correlation between variables and gas density or dust temperature.

Table A1 lists all of the sources in our sample for IRAM 30 m, NRO 45 m, and ALMA observations.

Table A2 lists the targeted lines covered by our IRAM 30 m and NRO 45 m observations.

Table A3 lists the line profile fitting results using the GAUSS method in the GILDAS package toward the P1, P2, and P3 of each source.

Table A4 lists the gas parameters of our target in this work derived by using different temperature measurements.
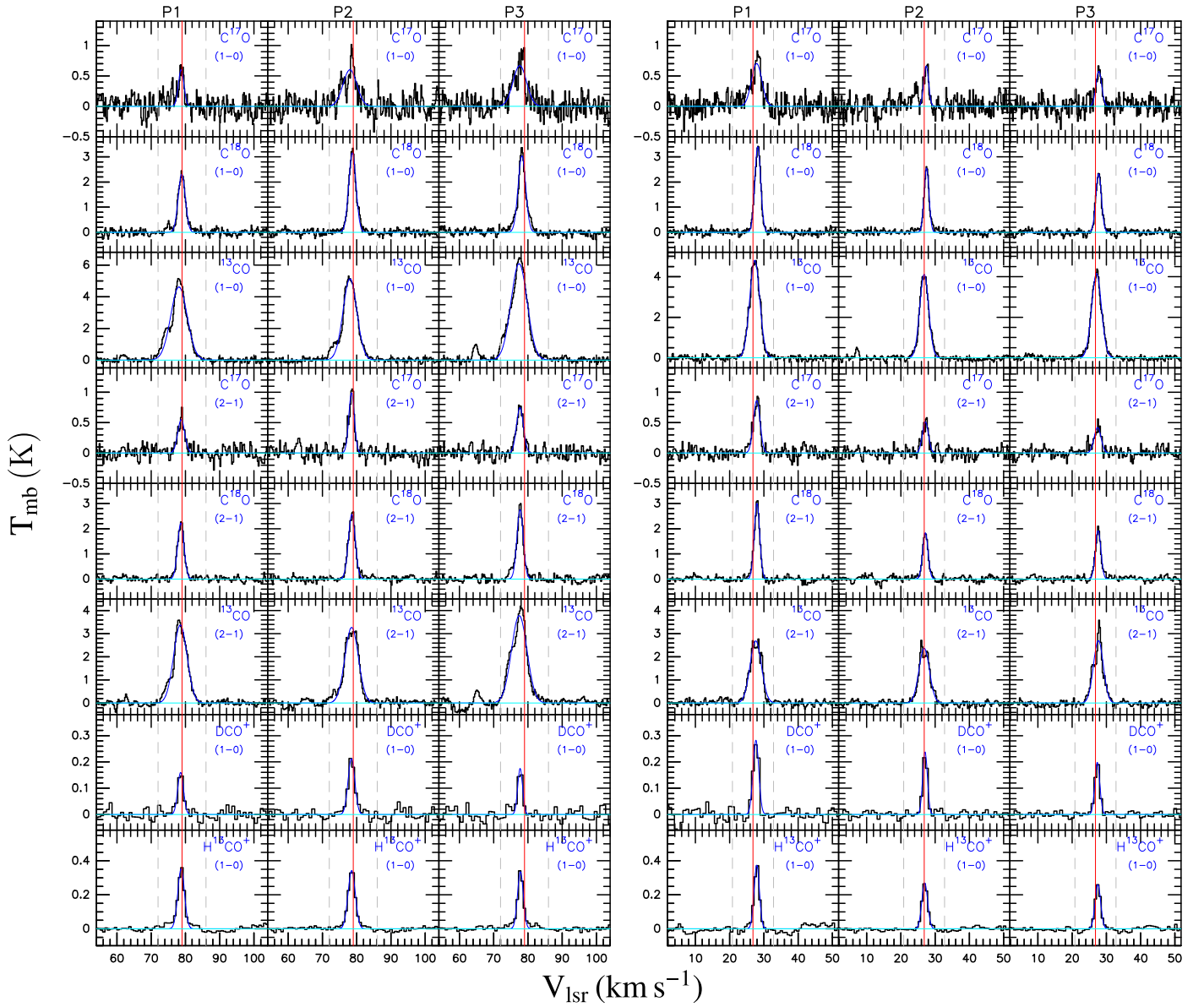
Figure A1. Profiles of the CO and HCO$^+$ isotopologue lines observed using the IRAM 30 m and NRO 45 m, averaged from a beam-sized region with the center toward P1, P2, and P3 of each source in the plane of the sky. All lines are extracted from images that we regridded to the same pixel size but whose native angular and velocity resolution we kept as in the observations (see beam information in Table A2). In each panel, two gray dashed vertical lines indicate the velocity range for which we integrate the intensity; the red vertical line indicates the V_{sys} of each source. The horizontal cyan line indicates the baseline ($T_{mb} = 0$ K).
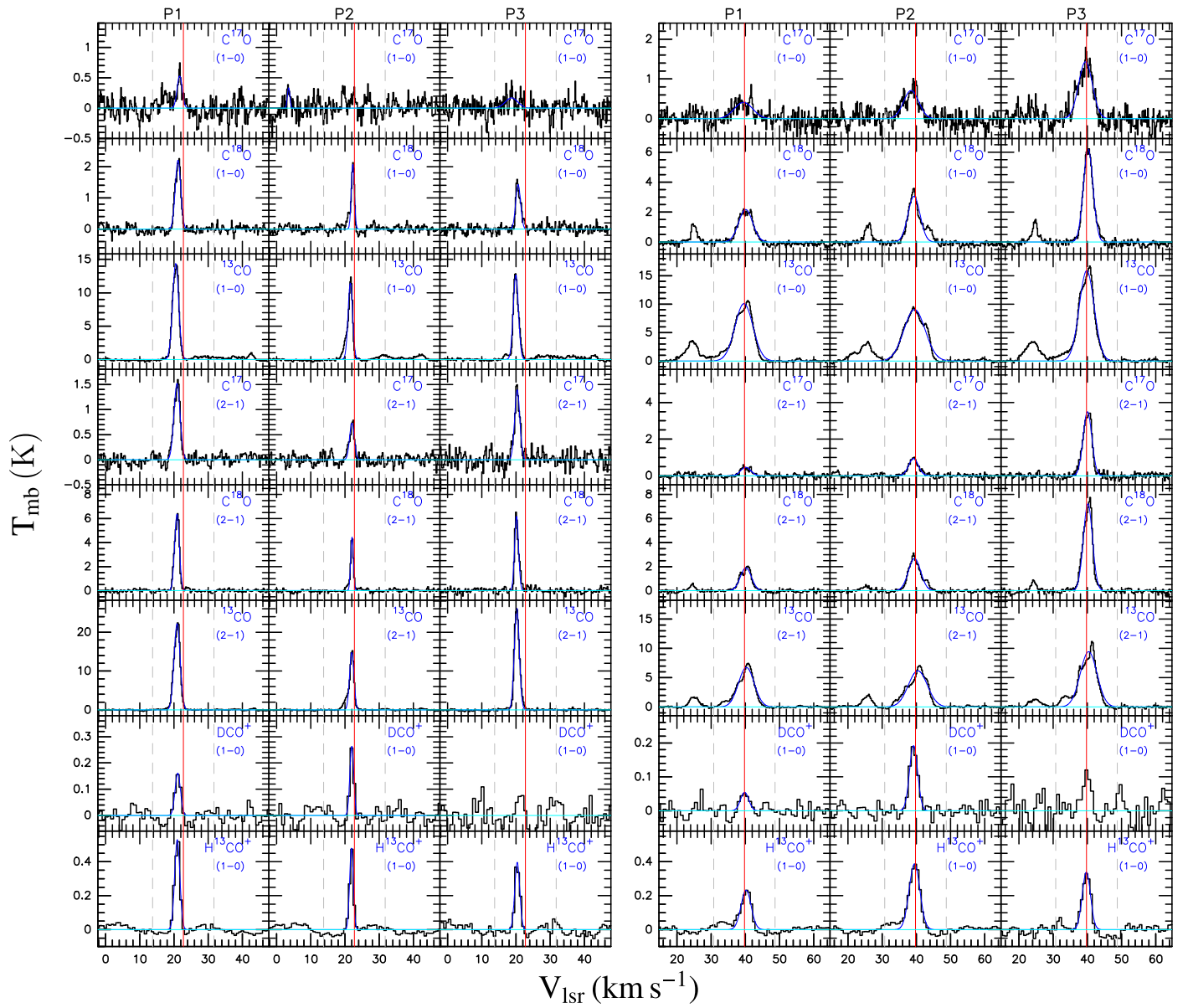
Figure A1. (Continued.)
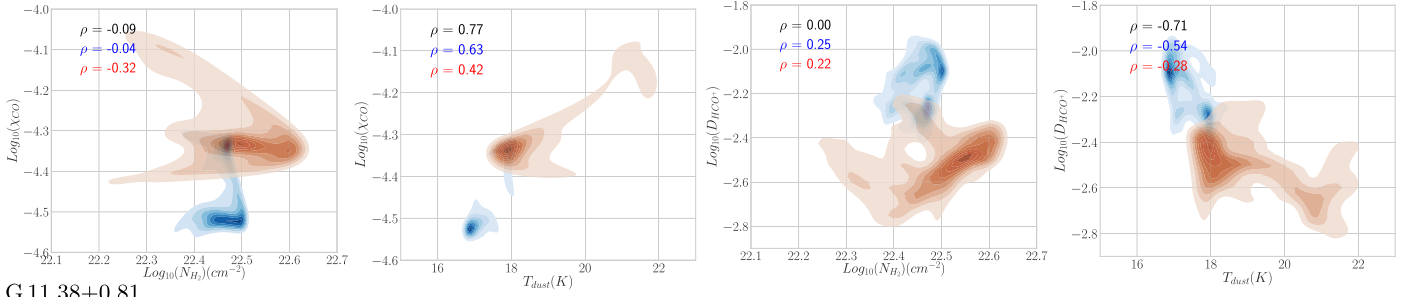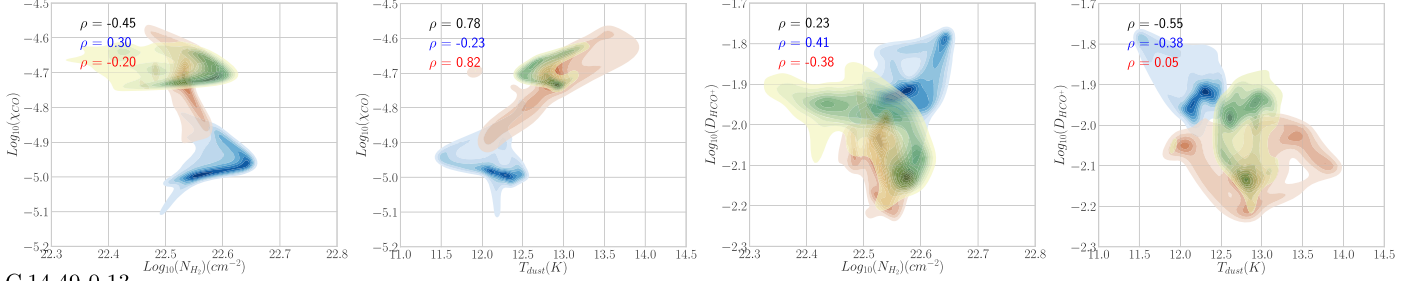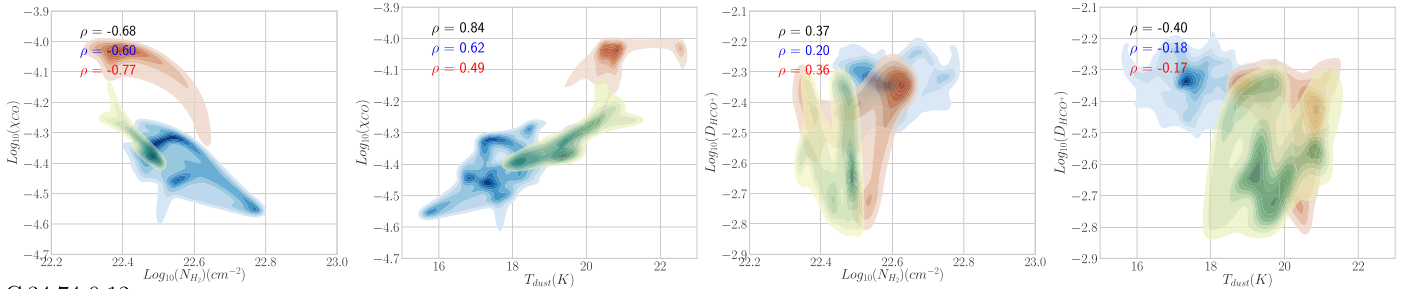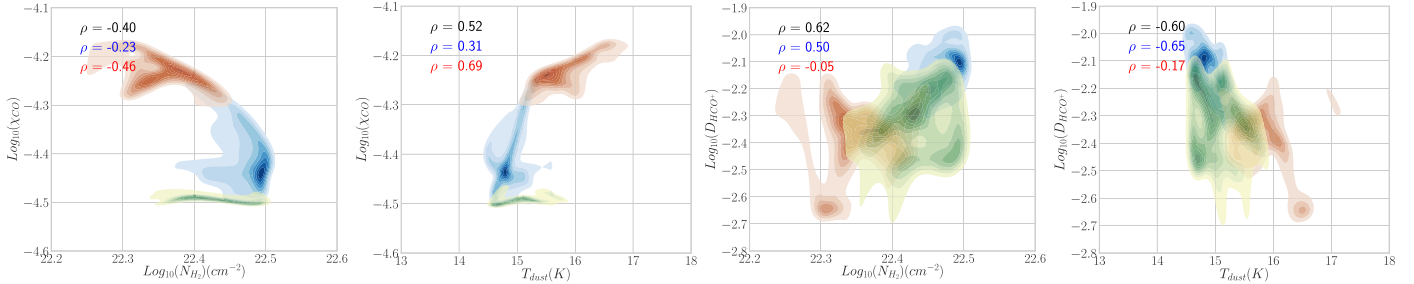
Figure A2. Possible correlation between variables and gas density or dust temperature. Values are extracted from pixels after smoothing the parameter maps to the same angular resolution (36″) and plotted with a bivariate Gaussian kernel density estimate as contours. The CO- and DCO$^+$-dominant zones are plotted in red and blue, with the Spearman's rank correlation coefficient ρ given in red and blue, respectively. The transition zone is plotted in yellowish-green. The Spearman's rank correlation coefficient ρ of the entire source is given in black. The pixels where the continuum at 870 μm shows $<5\sigma$ emission or DCO$^+$(1–0) shows $<3\sigma$ emission are blanked.

Table A1
Sources in Our Sample and Their Observation Parameters

Source[a]	R.A.[b] (J2000)	Decl.[b] (J2000)	d[c] (kpc)	R_{GC}[d] (kpc)	V_{sys} (km s^{-1})	rms$_{4.0mm}$[e] (K)	rms$_{3.4mm}$[f] (K)	rms$_{1.3mm}$[g] (K)
G011.0970–0.1093	$18^h10^m25^s70$	$-19°22'59''5$	3.0	4.9	29.8[h]	0.05	0.02	0.27
G011.3811+0.8103	$18^h07^m36^s41$	$-18°41'21''1$	2.8	5.2	26.8[i]	0.02	0.02	0.17
G012.9459–0.2488	$18^h14^m41^s50$	$-17°49'41''9$	3.0	5.0	34.0[j]	0.03	0.02	0.28
G012.9674–0.2380	$18^h14^m41^s69$	$-17°48'15''8$	3.0	4.9	35.0[k]	0.04	0.02	0.25
G014.1842–0.2280	$18^h17^m05^s14$	$-16°43'46''9$	3.1	4.8	39.7[j]	0.03	0.04	0.45
G014.2314–0.1758	$18^h16^m59^s23$	$-16°39'47''9$	3.0	4.9	37.5[h]	0.03	0.03	0.23
G014.4876–0.1274	$18^h17^m19^s03$	$-16°24'53''6$	3.2	4.9	39.7[h]	0.03	0.03	0.31
G014.6858–0.2234	$18^h18^m03^s67$	$-16°17'09''6$	3.0	5.0	37.7[h]	0.02	0.02	0.14
G014.7258–0.2031	$18^h18^m03^s96$	$-16°14'28''0$	3.1	5.0	37.5[h]	0.04	0.04	0.24
G015.2169–0.4267	$18^h19^m51^s19$	$-15°54'50''8$	1.9	6.1	22.7[l]	0.05	0.04	0.33
G015.5022–0.4201	$18^h20^m23^s28$	$-15°39'33''8$	3.2	5.0	39.7[j]	0.04	0.04	0.37
G016.3013–0.5251	$18^h22^m19^s90$	$-15°00'13''7$	3.2	5.2	38.3[h]	0.05	0.02	0.54
G018.8008–0.2958	$18^h26^m18^s94$	$-12°41'15''4$	5.0	4.3	65.5[j]	0.04	0.02	0.30
G018.9295–0.0289	$18^h25^m35^s64$	$-12°26'57''1$	3.3	5.2	43.6[m]	0.06	0.03	0.24
G022.5309–0.1927	$18^h32^m59^s64$	$-09°20'06''0$	5.0	4.3	75.9[h]	0.03	0.03	0.46
G022.6919–0.4519	$18^h34^m13^s61$	$-09°18'42''5$	4.9	4.3	76.8[h]	0.04	0.04	0.26
G022.7215–0.2733	$18^h33^m38^s38$	$-09°12'11''5$	4.6	4.4	72.8[h]	0.03	0.02	0.36
G024.5245–0.1397	$18^h36^m30^s98$	$-07°32'28''0$	5.7	4.1	90.3[l]	0.05	0.02	0.23
G028.2726–0.1666	$18^h43^m31^s18$	$-04°13'18''8$	4.5	4.7	79.6[i]	0.04	0.03	0.38
G028.3231–0.0676	$18^h42^m46^s60$	$-04°04'11''9$	4.6	4.7	79.5[n]	0.03	0.03	0.11
G028.5246–0.2519	$18^h44^m17^s14$	$-04°02'12''5$	4.7	4.5	87.3[i]	0.06	0.03	0.32
G028.5413–0.2371	$18^h44^m15^s79$	$-04°00'54''7$	4.6	4.6	84.3[i]	0.04	0.03	0.36
G034.7391–0.1197	$18^h55^m09^s70$	$+01°33'13''3$	4.7	5.2	79.0[h]	0.02	0.02	0.18
G034.7798–0.5671	$18^h56^m49^s73$	$+01°23'08''9$	2.2	6.4	41.3[j]	0.05	0.03	0.21

Notes.
[a] ATLASGAL name.
[b] OTF mapping center.
[c] Kinematic distance from Yuan et al. (2017) with an uncertainty of ±0.5 kpc.
[d] Galactocentric distance, calculated using Wenger et al. (2018).
[e] Measured by IRAM 30 m in main-beam temperature T_{mb} (K) directly from observations without smoothing, with an angular resolution of $\sim36''$ and velocity resolution of ~0.72 km s^{-1} for 4.0 mm lines.
[f] Measured by IRAM 30 m in main-beam temperature T_{mb} (K) directly from observations without smoothing, with an angular resolution of $\sim29''$ and velocity resolution of ~0.56 km s^{-1} for 3.4 mm lines.
[g] Measured by IRAM 30 m in main-beam temperature T_{mb} (K) directly from observations without smoothing, with an angular resolution of $\sim11''$ and velocity resolution of ~0.22 km s^{-1} for 1.3 mm lines.
[h] Wienen et al. (2012).
[i] Csengeri et al. (2014).
[j] Shirley et al. (2013).
[k] Single-pointed observation using the Submillimeter Telescope (SMT; Yuan et al. 2017).
[l] Dempsey et al. (2013).
[m] Purcell et al. (2012).
[n] Pilot study source, with line information given in Feng et al. (2019).

Table A2
Targeted Lines Covered by Our IRAM 30 m and NRO 45 m Observations

Mol.	Freq. (GHz)	Transition	$S\mu^{2a}$ (D^2)	E_u/k_B [a] (K)	n_{crit} (cm^{-3})[d] 10 K	20 K	n_{eff} (cm^{-3})[e] 10 K	15 K	20 K	Telescope	Beam
HCN	88.632	$J = 1$–0^c	26.8	4.2	4.7E+5	3.0E+5	8.4E+3	5.6E+3	4.5E+3	IRAM 30 m	29.3
$H^{13}CN$	86.340	$J = 1$–0^c	26.7	4.1	4.3E+5	2.7E+5	3.5E+5	2.2E+5	1.6E+5	IRAM 30 m	30.0
$HC^{15}N$	86.055	1–0	8.9	4.1	4.3E+5	2.7E+5	⋯	⋯	⋯	IRAM 30 m	30.1
DCN	72.415	$J = 1$–0^c	26.8	3.5	2.6E+5	1.6E+5	⋯	⋯	⋯	IRAM 30 m	35.8
HNC	90.664	1–0	9.3	4.3	1.4E+5	1.1E+5	3.7E+3	2.7E+3	2.3E+3	IRAM 30 m	28.6
$HN^{13}C$	87.091	1–0	7.3	4.2	9.6E+4	7.3E+4	⋯	⋯	⋯	IRAM 30 m	29.8
$H^{15}NC$	88.866	1–0	7.3	4.3	1.0E+5	7.8E+4	⋯	⋯	⋯	IRAM 30 m	29.2
DNC	76.306	1–0	9.3	3.7	8.2E+4	6.3E+4	⋯	⋯	⋯	IRAM 30 m	34.0
HCO^+	89.189	1–0	15.2	4.2	7.0E+4	4.7E+4	9.5E+2	6.4E+2	5.3E+2	IRAM 30 m	29.1
$H^{13}CO^+$	86.754	$J = 1$–0^b	15.2	4.2	6.2E+4	4.1E+4	3.9E+4	2.7E+4	2.2E+4	IRAM 30 m	29.9
$HC^{18}O^+$	85.162	1–0	15.2	4.1	4.2E+4	2.8E+4	⋯	⋯	⋯	IRAM 30 m	30.5
DCO^+	72.039	$J = 1$–0^b	14.5	3.5	3.2E+4	2.1E+4	⋯	⋯	⋯	IRAM 30 m	36.0
N_2H^+	93.173	$J = 1$–0^c	104.0	4.5	6.1E+4	4.1E+4	1.0E+4	6.7E+3	5.5E+3	IRAM 30 m	27.8
N_2D^+	77.109	$J = 1$–0^c	104.0	3.7	5.9E+4	3.9E+4	⋯	⋯	⋯	IRAM 30 m	33.6
$C^{18}O$	219.560	2–1	0.02	15.8	4.7E+3	3.8E+3	⋯	⋯	⋯	IRAM 30 m	11.8
^{13}CO	220.400	2–1	0.02	15.9	4.8E+3	3.8E+3	⋯	⋯	⋯	IRAM 30 m	11.8
$C^{17}O$	224.714	2–1	0.02	16.2	5.1E+3	4.1E+3	⋯	⋯	⋯	IRAM 30 m	11.5
$C^{18}O$	109.782	1–0	0.01	5.3	7.5E+2	4.8E+2	⋯	⋯	⋯	NRO 45 m	16.4
^{13}CO	110.201	1–0	0.01	5.3	7.6E+2	4.8E+2	⋯	⋯	⋯	NRO 45 m	16.4
$C^{17}O$	112.359	1–0	0.01	5.4	8.2E+2	5.2E+2	⋯	⋯	⋯	NRO 45 m	16.1
H_2CO	72.838	$1_{0,1}$–$0_{0,0}$	5.4	3.5	4.5E+4	2.8E+4	5.0E+4	3.2E+4	2.6E+4	IRAM 30 m	35.6
H_2CO	218.222	$3_{0,3}$–$2_{0,2}$	16.3	21.0	9.7E+5	7.8E+5	1.5E+5	8.2E+4	6.3E+4	IRAM 30 m	11.9
H_2CO	218.476	$3_{2,2}$–$2_{2,1}$	9.1	68.1	3.5E+5	3.2E+5	⋯	⋯	⋯	IRAM 30 m	11.9
H_2CO	218.760	$3_{2,1}$–$2_{2,0}$	9.1	68.1	3.5E+5	3.2E+5	⋯	⋯	⋯	IRAM 30 m	11.9
CH_3OH	76.510	$5_{0,5}$–$4_{1,3}$ E	1.9	47.9	2.5E+3	2.1E+3	⋯	⋯	⋯	IRAM 30 m	33.9
CH_3OH	84.521	$5_{-1, 5}$–$4_{0,4}$ E	3.1	40.4	6.1E+3	5.1E+3	⋯	⋯	⋯	IRAM 30 m	30.7
CH_3OH	218.440	$4_{2, 2}$–$3_{1,2}$ E	3.5	45.5	1.6E+5	1.3E+5	⋯	⋯	⋯	IRAM 30 m	11.9
CH_2DOH	89.408	$2_{0,2}$–$1_{0,1}$ e0	1.2	6.4	4.1E+4	3.1E+4	⋯	⋯	⋯	IRAM 30 m	29.0
OCS	85.139	7–6	3.6	16.3	4.1E+3	3.3E+3	⋯	⋯	⋯	IRAM 30 m	30.5
c-C_3H_2	85.339	$2_{1,2}$–$1_{0,1}$	48.1	6.4	3.2E+5	1.6E+5	⋯	⋯	⋯	IRAM 30 m	30.4
CH_3C_2H	85.456	5_1–4_1	1.8	19.5	⋯	⋯	⋯	⋯	⋯	IRAM 30 m	30.3
CH_3C_2H	85.457	5_0–4_0	1.9	12.3	⋯	⋯	⋯	⋯	⋯	IRAM 30 m	30.3
NH_2D	85.926	$1_{1,1}$ 0s–$1_{0,1}$ 0a	28.6	20.7	5.6E+4	4.8E+4	⋯	⋯	⋯	IRAM 30 m	30.2
SiO	86.847	2–1	19.2	6.3	6.7E+4	5.4E+4	⋯	⋯	⋯	IRAM 30 m	29.9
C_2H	87.284	$N = 1$–0, $J = 3/2$–$1/2$, $F = 1$–1	0.1	4.2	4.2E+3	2.4E+3	⋯	⋯	⋯	IRAM 30 m	29.7
C_2H	87.317	$N = 1$–0, $J = 3/2$–$1/2$, $F = 2$–1	1.0	4.2	2.7E+4	1.5E+4	⋯	⋯	⋯	IRAM 30 m	29.7
C_2H	87.329	$N = 1$–0, $J = 3/2$–$1/2$, $F = 1$–0	0.5	4.2	2.1E+4	1.2E+4	⋯	⋯	⋯	IRAM 30 m	29.7
C_2H	87.402	$N = 1$–0, $J = 1/2$–$1/2$, $F = 1$–1	0.5	4.2	1.7E+4	1.0E+4	⋯	⋯	⋯	IRAM 30 m	29.7
C_2H	87.407	$N = 1$–0, $J = 1/2$–$1/2$, $F = 0$–1	0.2	4.2	1.8E+4	1.2E+4	⋯	⋯	⋯	IRAM 30 m	29.7
C_2H	87.446	$N = 1$–0, $J = 1/2$–$1/2$, $F = 1$–0	0.1	4.2	3.5E+3	2.1E+3	⋯	⋯	⋯	IRAM 30 m	29.7
HNCO	87.925	$4_{0,4}$–$3_{0,3}$	30.8	10.5	8.7E+4	5.3E+4	⋯	⋯	⋯	IRAM 30 m	29.5
HC_3N	90.979	10–9	138.7	24.0	1.6E+5	1.2E+5	4.3E+5	7.2E+4	4.3E+4	IRAM 30 m	28.5
^{13}CS	92.494	2–1	15.3	6.7	3.0E+5	2.3E+5	⋯	⋯	⋯	IRAM 30 m	28.0

Notes.

[a] Line spectroscopic parameters are given according to catalogs including the JPL (Pickett et al. 1998; http://spec.jpl.nasa.gov) and CDMS (Müller et al. 2005; http://www.astro.uni-koeln.de/cdms/catalog).

[b] Hyperfine splittings are recorded in JPL and CDMS but not resolved in our observations, so the sum of $S\mu^2$ is used for the rotational transitions to calculate the total column density.

[c] Hyperfine splittings are resolved in our observations, and only the sum of $S\mu^2$ is needed for the rotational transitions to calculate the total column density.

[d] The critical density of each transition n_{crit} is derived from the Einstein coefficient A_{ij} and the collision rate C_{ij} at 10–20 K given by LAMDA (Schöier et al. 2005). We assume that the deuterated lines have the same C_{ij} as their hydrogenated counterparts.

[e] The effective excitation density at kinetic temperatures of 10–20 K from Shirley (2015); "⋯" indicates an unrecorded value.

Table A3
The Best-fit Parameters (Line Width Δv (km s^{-1}) and Integrated Intensity $\int T_B(v)dv$ (K km s^{-1})) for Lines in Figure A1 Given by GILDAS

Source	Line[a]	Freq.[b] (GHz)	θ[c] (arcsec)	P1[d] (km s^{-1})	P1[d] (K km s^{-1})	P2[d] (km s^{-1})	P2[d] (K km s^{-1})	P3[d] (km s^{-1})	P3[d] (K km s^{-1})	Velocity Range[e] [km s^{-1}, km s^{-1}]	σ[f] (K km s^{-1})
G15.22–0.43	^{13}CO (2 − 1)	220.398	11.8	2.1 ± 0.0	49.08 ± 0.16	1.5 ± 0.0	23.72 ± 0.27	1.7 ± 0.0	47.65 ± 0.21	[14, 32]	1.41
	C^{18}O (2 − 1)	219.560	11.8	1.6 ± 0.0	10.95 ± 0.11	0.9 ± 0.0	4.41 ± 0.09	1.3 ± 0.0	8.88 ± 0.16	[14, 32]	1.16
	C^{17}O (2 − 1)	224.714	11.5	2.1 ± 0.1	3.39 ± 0.10	1.6 ± 0.2	1.28 ± 0.10	1.8 ± 0.1	2.62 ± 0.15	[14, 32]	0.94
	H^{13}CO$^+$ (1 − 0)	86.754	29.9	1.8 ± 0.1	1.01 ± 0.03	1.3 ± 0.1	0.65 ± 0.03	1.7 ± 0.1	0.73 ± 0.04	[14, 32]	0.35
	DCO$^+$ (1 − 0)	72.039	36.0	1.9 ± 0.3	0.32 ± 0.04	1.3 ± 0.1	0.38 ± 0.04	...[g]	σ = 0.04[g]	[14, 32]	0.09
	^{13}CO (1 − 0)	110.201	16.4	2.1 ± 0.0	32.14 ± 0.26	1.6 ± 0.0	19.04 ± 0.26	1.8 ± 0.0	23.67 ± 0.27	[14, 32]	8.57
	C^{18}O (1 − 0)	109.783	16.4	1.9 ± 0.0	4.39 ± 0.10	1.1 ± 0.0	2.33 ± 0.08	1.7 ± 0.1	2.54 ± 0.10	[14, 32]	0.67
	C^{17}O (1 − 0)	112.359	16.0	1.8 ± 0.6	0.99 ± 0.19	0.9 ± 0.3	0.31 ± 0.10	4.4 ± 1.1	0.79 ± 0.18	[14, 32]	1.43
G11.38+0.81	^{13}CO (2 − 1)	220.398	11.8	3.9 ± 0.1	11.28 ± 0.16	3.6 ± 0.1	9.14 ± 0.15	3.4 ± 0.1	9.77 ± 0.14	[21, 33]	0.55
	C^{18}O (2 − 1)	219.560	11.8	1.9 ± 0.0	6.02 ± 0.10	1.8 ± 0.1	3.59 ± 0.11	1.9 ± 0.1	3.86 ± 0.10	[21, 33]	0.59
	C^{17}O (2 − 1)	224.714	11.5	2.3 ± 0.1	2.13 ± 0.10	2.1 ± 0.2	1.13 ± 0.08	2.4 ± 0.3	1.07 ± 0.10	[21, 33]	0.53
	H^{13}CO$^+$ (1 − 0)	86.754	29.9	1.8 ± 0.1	0.74 ± 0.03	2.0 ± 0.1	0.57 ± 0.02	1.9 ± 0.1	0.54 ± 0.02	[21, 33]	0.13
	DCO$^+$ (1 − 0)	72.039	36.0	2.0 ± 0.1	0.60 ± 0.04	1.6 ± 0.1	0.41 ± 0.02	1.7 ± 0.1	0.36 ± 0.02	[21, 33]	0.08
	^{13}CO (1 − 0)	110.201	16.4	3.5 ± 0.0	17.71 ± 0.12	3.1 ± 0.0	13.45 ± 0.13	3.4 ± 0.0	14.97 ± 0.11	[21, 33]	11.18
	C^{18}O (1 − 0)	109.783	16.4	2.0 ± 0.0	7.31 ± 0.10	1.7 ± 0.0	4.60 ± 0.08	1.9 ± 0.0	4.79 ± 0.09	[21, 33]	1.27
	C^{17}O (1 − 0)	112.359	16.0	3.6 ± 0.4	2.70 ± 0.20	1.7 ± 0.2	1.18 ± 0.12	2.0 ± 0.2	1.22 ± 0.12	[21, 33]	1.16
G14.49–0.13	^{13}CO (2 − 1)	220.398	11.8	5.4 ± 0.1	38.74 ± 0.87	6.5 ± 0.2	42.87 ± 1.06	5.8 ± 0.1	57.89 ± 0.97	[31, 49]	1.86
	C^{18}O (2 − 1)	219.560	11.8	3.8 ± 0.1	7.69 ± 0.21	4.2 ± 0.1	12.04 ± 0.22	3.1 ± 0.0	24.20 ± 0.29	[31, 49]	1.20
	C^{17}O (2 − 1)	224.714	11.5	3.5 ± 0.3	1.69 ± 0.13	3.3 ± 0.2	3.34 ± 0.15	3.0 ± 0.1	11.17 ± 0.17	[31, 49]	0.96
	H^{13}CO$^+$ (1 − 0)	86.754	29.9	3.5 ± 0.2	0.86 ± 0.05	3.7 ± 0.1	1.53 ± 0.05	2.8 ± 0.2	1.02 ± 0.06	[31, 49]	0.28
	DCO$^+$ (1 − 0)	72.039	36.0	2.9 ± 0.7	0.17 ± 0.04	2.8 ± 0.2	0.57 ± 0.04	2.6 ± 0.8	0.32 ± 0.09	[31, 49]	0.12
	^{13}CO (1 − 0)	110.201	16.4	6.2 ± 0.2	66.23 ± 1.76	7.3 ± 0.2	70.33 ± 1.82	5.1 ± 0.1	86.92 ± 1.68	[31, 49]	46.70
	C^{18}O (1 − 0)	109.783	16.4	4.8 ± 0.2	11.10 ± 0.39	4.2 ± 0.2	13.56 ± 0.46	3.3 ± 0.1	21.86 ± 0.38	[31, 49]	5.68
	C^{17}O (1 − 0)	112.359	16.0	6.4 ± 0.7	2.79 ± 0.28	5.2 ± 0.4	3.95 ± 0.28	4.8 ± 0.2	7.26 ± 0.30	[31, 49]	2.19
G34.74–0.12	^{13}CO (2 − 1)	220.398	11.8	4.6 ± 0.1	16.70 ± 0.19	4.7 ± 0.1	16.22 ± 0.22	5.4 ± 0.1	21.63 ± 0.34	[72, 85]	0.68
	C^{18}O (2 − 1)	219.560	11.8	2.2 ± 0.1	5.21 ± 0.11	2.4 ± 0.0	6.50 ± 0.11	2.2 ± 0.1	6.40 ± 0.14	[72, 85]	0.61
	C^{17}O (2 − 1)	224.714	11.5	2.4 ± 0.2	1.42 ± 0.12	1.9 ± 0.1	2.03 ± 0.10	2.4 ± 0.2	1.88 ± 0.10	[72, 85]	0.56
	H^{13}CO$^+$ (1 − 0)	86.754	29.9	2.3 ± 0.1	0.87 ± 0.03	2.5 ± 0.1	0.92 ± 0.02	2.0 ± 0.1	0.71 ± 0.02	[72, 85]	0.18
	DCO$^+$ (1 − 0)	72.039	36.0	2.0 ± 0.3	0.34 ± 0.04	2.3 ± 0.2	0.53 ± 0.04	1.7 ± 0.2	0.31 ± 0.04	[72, 85]	0.19
	^{13}CO (1 − 0)	110.201	16.4	5.6 ± 0.1	27.72 ± 0.20	4.8 ± 0.0	25.95 ± 0.17	5.6 ± 0.1	36.06 ± 0.36	[72, 85]	14.26
	C^{18}O (1 − 0)	109.783	16.4	2.4 ± 0.1	5.98 ± 0.13	2.5 ± 0.0	8.43 ± 0.11	2.6 ± 0.1	8.44 ± 0.13	[72, 85]	1.59
	C^{17}O (1 − 0)	112.359	16.0	1.9 ± 0.4	1.22 ± 0.17	4.7 ± 0.4	3.03 ± 0.23	4.6 ± 0.4	3.32 ± 0.22	[72, 85]	1.57

Notes.
[a] Lines are extracted from images by averaging a beam-sized region centered at P1, P2, and P3 in the plane of the sky. All line images have the same pixel size, but whose native angular and velocity resolution we kept as in the observations.
[b] Rest frequency is given from the main line of the hyperfine splittings.
[c] Angular resolution from observations.
[d] Uncertainties on the measured intensities are typically ⩽10%.
[e] The velocity range we integrate for individual lines to obtain their intensity maps is in Figure A1.
[f] The σ rms on the molecular line intensity maps is in Figure A1.
[g] Line emission <3σ rms.

Table A4
Gas Parameters of Our Targets

Properties		Source	G15.22–0.43 Case A[a]	G15.22–0.43 Case B[b]	G11.38+0.81 Case A[a]	G11.38+0.81 Case B[b]	G14.49–0.13 Case A[a]	G14.49–0.13 Case B[b]	G34.74–0.12 Case A[a]	G34.74–0.12 Case B[b]
$\theta = 16''-20''$										
$N_{C^{18}O}$	$(\times 10^{15}\,cm^{-2})$	P1	3.1 ± 0.6	2.6 ± 0.3	3.4 ± 1.7	10.9 ± 4.6	12.4 ± 6.5	22.8 ± 4.5	6.7 ± 2.9	9.7 ± 2.6
		P2	6.1 ± 0.1	5.5 ± 0.4	5.0 ± 2.5	13.7 ± 5.0	10.5 ± 6.3	22.5 ± 4.6	5.3 ± 2.2	6.6 ± 1.3
		P3	5.5 ± 0.2	4.8 ± 0.3	3.2 ± 1.3	4.4 ± 0.8	21.7 ± 10.5	26.6 ± 3.2	7.8 ± 4.0	15.6 ± 4.7
$f_D(C^{18}O)$[g]		P1	4.1 ± 0.9		11.9 ± 6.2		4.8 ± 2.5		3.1 ± 1.3	
		P2	3.1 ± 0.1		6.7 ± 3.3		3.3 ± 2.0		3.7 ± 1.6	
		P3	1.3 ± 0.1		7.9 ± 3.4		1.7 ± 0.9		1.2 ± 0.6	

Properties		Source	G15.22–0.43 Case C[c]	Case D[d]	Case E[e]	G11.38+0.81 Case C[c]	Case D[d]	Case E[e]	G14.49–0.13 Case C[c]	Case D[d]	Case E[e]	G34.74–0.12 Case C[c]	Case D[d]	Case E[e]
$\theta \sim 35''$													
$N_{C^{18}O}$	$(\times 10^{15}\,cm^{-2})$	P1	2.5 ± 0.1	$\cdots$[f]	3.5 ± 2.7	1.5 ± 0.3	$\cdots$[f]	1.4 ± 0.9	5.2 ± 0.9	5.2 ± 0.5	5.3 ± 3.8	3.6 ± 0.1	3.4 ± 0.4	3.8 ± 2.6
		P2	4.9 ± 0.1	$\cdots$[f]	5.3 ± 2.8	2.2 ± 0.2	$\cdots$[f]	1.8 ± 1.1	4.0 ± 0.9	4.0 ± 1.5	4.3 ± 3.5	2.8 ± 0.1	2.7 ± 0.3	3.0 ± 2.4
		P3	3.8 ± 0.1	$\cdots$[f]	4.7 ± 3.1	1.7 ± 0.3	$\cdots$[f]	1.7 ± 1.2	7.0 ± 0.9	7.7 ± 3.3	7.9 ± 4.9	3.4 ± 0.1	3.3 ± 1.1	3.9 ± 2.9
$f_D(C^{18}O)$[g]		P1	4.1 ± 0.1	$\cdots$[f]	2.9 ± 2.1	12.8 ± 2.3	$\cdots$[f]	13.6 ± 8.9	5.4 ± 1.0	8.3 ± 0.8	5.3 ± 3.7	3.8 ± 0.1	5.0 ± 0.7	3.6 ± 2.4
		P2	2.7 ± 0.1	$\cdots$[f]	2.5 ± 1.3	7.6 ± 0.9	$\cdots$[f]	9.0 ± 5.3	3.5 ± 0.8	5.3 ± 1.9	3.3 ± 2.3	4.5 ± 0.1	5.9 ± 0.7	4.1 ± 2.9
		P3	1.5 ± 0.1	$\cdots$[f]	1.2 ± 0.8	9.2 ± 1.6	$\cdots$[f]	8.9 ± 6.2	2.8 ± 0.4	3.5 ± 1.5	2.5 ± 1.5	2.1 ± 0.1	2.0 ± 0.7	1.9 ± 1.3
$N_{H^{13}CO^+}$	$(\times 10^{12}\,cm^{-2})$	P1	1.4 ± 0.1	$\cdots$[f]	2.5 ± 1.9	0.7 ± 0.3	$\cdots$[f]	1.3 ± 0.9	2.6 ± 0.1	2.7 ± 0.3	3.3 ± 1.3	1.4 ± 0.1	1.4 ± 0.3	2.3 ± 1.2
		P2	2.3 ± 0.1	$\cdots$[f]	3.1 ± 1.5	1.1 ± 0.3	$\cdots$[f]	2.0 ± 1.1	1.5 ± 0.1	1.5 ± 0.5	1.9 ± 1.0	1.5 ± 0.1	1.4 ± 0.2	2.8 ± 1.6
		P3	1.4 ± 0.1	$\cdots$[f]	2.0 ± 1.3	0.7 ± 0.3	$\cdots$[f]	1.6 ± 1.1	1.8 ± 0.1	1.6 ± 0.6	2.1 ± 1.0	1.4 ± 0.1	1.3 ± 0.4	2.2 ± 1.3
N_{DCO^+}	$(\times 10^{11}\,cm^{-2})$	P1	5.8 ± 0.6	$\cdots$[f]	12.7 ± 9.6	4.9 ± 1.3	$\cdots$[f]	10.6 ± 6.2	6.1 ± 0.5	6.2 ± 1.5	7.6 ± 2.9	5.9 ± 0.5	6.0 ± 1.4	10.3 ± 5.7
		P2	4.1 ± 0.6	$\cdots$[f]	5.7 ± 2.9	5.0 ± 1.4	$\cdots$[f]	9.5 ± 5.2	<1.2[i]	<0.8[i]	<1.1[i]	<2.4[i]	<2.3[i]	<3.5[i]
		P3	<2.1[i]	$\cdots$[f]	<3.4[i]	2.4 ± 1.4	$\cdots$[f]	<5.5	3.6 ± 0.5	2.9 ± 1.7	3.9 ± 1.8	<3.3[i]	<2.8[i]	<4.1[i]
D_{HCO^+}[h]		P1	$1.0\% \pm 0.1\%$	$\cdots$[f]	$1.0\% \pm 0.8\%$	$1.6\% \pm 0.8\%$	$\cdots$[f]	$1.7\% \pm 1.3\%$	$0.5\% \pm 0.1\%$	$0.5\% \pm 0.1\%$	$0.5\% \pm 0.3\%$	$1.0\% \pm 0.1\%$	$0.9\% \pm 0.3\%$	$1.0\% \pm 0.7\%$
		P2	$0.4\% \pm 0.1\%$	$\cdots$[f]	$0.4\% \pm 0.2\%$	$1.0\% \pm 0.3\%$	$\cdots$[f]	$1.0\% \pm 0.8\%$	$<0.1\%$[i]	$<0.1\%$[i]	$<0.1\%$[i]	$<0.4\%$[i]	$<0.4\%$[i]	$<0.4\%$[i]
		P3	$<0.4\%$[i]	$\cdots$[f]	$<0.4\%$[i]	$<0.7\%$[i]	$\cdots$[f]	$<0.7\%$[i]	$0.4\% \pm 0.1\%$	$0.4\% \pm 0.2\%$	$0.4\% \pm 0.3\%$	$<0.5\%$[i]	$<0.5\%$[i]	$<0.6\%$[i]

Notes. Here P1, P2, and P3 denote the DCO^+-dominant, transition, and CO-dominant zones, respectively.

[a] Use T_{dust} and derive from the (2–1)/(1–0) lines of $C^{18}O$ at an angular resolution of $18''$ or $20''$.

[b] Use the best fit of the (2–1)/(1–0) lines of $C^{18}O$ from RADEX at an angular resolution of $16''.4$.

[c] Use T_{dust} and derive from the $C^{18}O(2-1)$ line at an angular resolution of $34''.7$.

[d] Use T_{kin} (p–NH_3) at an angular resolution of $34''.7$.

[e] Use T_{rot}(p–H_2CO) at an angular resolution of $35''.6$.

[f] Here "$\cdots$" indicates the location where we do not have NH_3 observations.

[g] The $C^{18}O$ depletion is derived by assuming the expected abundance with respect to H_2 as Equations (1)–(2) and assuming a gas-to-dust mass ratio $\log(\gamma) = 0.087 R_{GC}(kpc) + 1.44$ (Draine 2011; Giannetti et al. 2017a).

[h] The D-fraction is derived from the $DCO^+(1-0)$ and $H^{13}CO^+(1-0)$ lines by assuming that they are optically thin, have the same beam filling toward each pixel, and have a constant fraction of $\mathcal{R}_{^{12}C/^{13}C} \sim 6.1 R_{GC}(kpc) + 14.3$ (Giannetti et al. 2014).

[i] An upper limit is given when the detected $DCO^+(1-0)$ shows $<3\sigma$ emission.

ORCID iDs

S. Feng (冯思轶) ⓘ https://orcid.org/0000-0002-4707-8409
D. Li ⓘ https://orcid.org/0000-0003-3010-7661
P. Caselli ⓘ https://orcid.org/0000-0003-1481-7911
F. Du ⓘ https://orcid.org/0000-0002-7489-0179
Y. Lin ⓘ https://orcid.org/0000-0001-9299-5479
O. Sipilä ⓘ https://orcid.org/0000-0002-9148-1625
H. Beuther ⓘ https://orcid.org/0000-0002-1700-090X
Patricio Sanhueza ⓘ https://orcid.org/0000-0002-7125-7685
K. Tatematsu ⓘ https://orcid.org/0000-0002-8149-8546
S. Y. Liu ⓘ https://orcid.org/0000-0003-4603-7119
Q. Zhang ⓘ https://orcid.org/0000-0003-2384-6589
Y. Wang ⓘ https://orcid.org/0000-0003-2226-4384
T. Hogge ⓘ https://orcid.org/0000-0002-7211-7078
I. Jimenez-Serra ⓘ https://orcid.org/0000-0003-4493-8714
X. Lu ⓘ https://orcid.org/0000-0003-2619-9305
T. Liu ⓘ https://orcid.org/0000-0002-5286-2564
K. Wang (王科) ⓘ https://orcid.org/0000-0002-7237-3856
Z. Y. Zhang ⓘ https://orcid.org/0000-0002-7299-2876
S. Zahorecz ⓘ https://orcid.org/0000-0001-6149-1278
G. Li ⓘ https://orcid.org/0000-0003-3144-1952
H. B. Liu ⓘ https://orcid.org/0000-0003-2300-2626
J. Yuan ⓘ https://orcid.org/0000-0001-8060-3538

References

Aikawa, Y. 2013, ChRv, 113, 8961
Aikawa, Y., Furuya, K., Hincelin, U., & Herbst, E. 2018, ApJ, 855, 119
Aikawa, Y., Herbst, E., Roberts, H., & Caselli, P. 2005, ApJ, 620, 330
Aikawa, Y., Wakelam, V., Hersant, F., Garrod, R. T., & Herbst, E. 2012, ApJ, 760, 40
Ao, Y., Henkel, C., Menten, K. M., et al. 2013, A&A, 550, A135
Bacmann, A., Lefloch, B., Ceccarelli, C., et al. 2003, ApJL, 585, L55
Barnes, A. T., Kong, S., Tan, J. C., et al. 2016, MNRAS, 458, 1990
Benjamin, R. A., Churchwell, E., Babler, B. L., et al. 2003, PASP, 115, 953
Bergin, E. A., Alves, J., Huard, T., & Lada, C. J. 2002, ApJL, 570, L101
Beuther, H., Churchwell, E. B., McKee, C. F., & Tan, J. C. 2007, in Protostars and Planets V, ed. B. Reipurth, D. Jewitt, & K. Keil (Tucson, AZ: Univ. Arizona Press), 165
Beuther, H., Henning, T., Linz, H., et al. 2015, A&A, 581, A119
Bonnell, I. A., & Bate, M. R. 2006, MNRAS, 370, 488
Bonnell, I. A., Vine, S. G., & Bate, M. R. 2004, MNRAS, 349, 735
Bovino, S., Ferrada-Chamorro, S., Lupi, A., et al. 2019, ApJ, 887, 224
Bovino, S., Grassi, T., Schleicher, D. R. G., & Caselli, P. 2017, ApJL, 849, L25
Burkert, A., & Hartmann, L. 2004, ApJ, 616, 288
Carigi, L., Peimbert, M., Esteban, C., & García-Rojas, J. 2005, ApJ, 623, 213
Caselli, P., Bizzocchi, L., Keto, E., et al. 2017, A&A, 603, L1
Caselli, P., Vastel, C., Ceccarelli, C., et al. 2008, A&A, 492, 703
Caselli, P., Walmsley, C. M., Tafalla, M., Dore, L., & Myers, P. C. 1999, ApJL, 523, L165
Caselli, P., Walmsley, C. M., Zucconi, A., et al. 2002a, ApJ, 565, 331
Caselli, P., Walmsley, C. M., Zucconi, A., et al. 2002b, ApJ, 565, 344
Ceccarelli, C., Caselli, P., Bockelée-Morvan, D., et al. 2014, in Protostars and Planets VI, ed. H. Beuther et al. (Tucson, AZ: Univ. Arizona Press), 859
Ceccarelli, C., Caselli, P., Herbst, E., Tielens, A. G. G. M., & Caux, E. 2007, in Protostars and Planets V, ed. B. Reipurth, D. Jewitt, & K. Keil (Tucson, AZ: Univ. Arizona Press), 47
Chen, H.-R., Liu, S.-Y., Su, Y.-N., & Zhang, Q. 2010, ApJL, 713, L50
Chevance, M., Kruijssen, J. M. D., Vazquez-Semadeni, E., et al. 2020, SSRv, 216, 50
Christie, H., Viti, S., Yates, J., et al. 2012, MNRAS, 422, 968
Churchwell, E., Sievers, A., & Thum, C. 2010, A&A, 513, A9
Cohen, J. 1988, Statistical Power Analysis for the Behavioral Sciences (New York: Routledge)
Contreras, Y., Sanhueza, P., Jackson, J. M., et al. 2018, ApJ, 861, 14
Crapsi, A., Caselli, P., Walmsley, C. M., et al. 2005, ApJ, 619, 379
Crapsi, A., Caselli, P., Walmsley, M. C., & Tafalla, M. 2007, A&A, 470, 221

Csengeri, T., Urquhart, J. S., Schuller, F., et al. 2014, A&A, 565, A75
Dempsey, J. T., Thomas, H. S., & Currie, M. J. 2013, ApJS, 209, 8
Draine, B. T. 2011, Physics of the Interstellar and Intergalactic Medium (Princeton, NJ: Princeton Univ. Press)
Du, F. 2020, arXiv:2007.11294
Dunham, M. M., Crapsi, A., Evans, N. J., II, et al. 2008, ApJS, 179, 249
Estalella, R. 2017, PASP, 129, 025003
Esteban, C., & García-Rojas, J. 2018, MNRAS, 478, 2315
Evans, N. I. 2003, in SFChem 2002: Chemistry as a Diagnostic of Star Formation, ed. C. L. Curry & M. Fich (Ottawa: NRC Press), 157
Feng, S., Beuther, H., Zhang, Q., et al. 2016a, A&A, 592, A21
Feng, S., Beuther, H., Zhang, Q., et al. 2016b, ApJ, 828, 100
Feng, S., Caselli, P., Wang, K., et al. 2019, ApJ, 883, 202
Feroz, F., & Hobson, M. P. 2008, MNRAS, 384, 449
Feroz, F., Hobson, M. P., & Bridges, M. 2009, MNRAS, 398, 1601
Feroz, F., Hobson, M. P., Cameron, E., & Pettitt, A. N. 2019, OJAp, 2, 10
Fontani, F., Giannetti, A., Beltrán, M. T., et al. 2012, MNRAS, 423, 2342
Fontani, F., Sakai, T., Furuya, K., et al. 2014, MNRAS, 440, 448
Frerking, M. A., Langer, W. D., & Wilson, R. W. 1982, ApJ, 262, 590
Furuya, K., Aikawa, Y., Hincelin, U., et al. 2015, A&A, 584, A124
Garrod, R. T. 2013, ApJ, 765, 60
Garrod, R. T., Weaver, S. L. W., & Herbst, E. 2008, ApJ, 682, 283
Gerlich, D., & Schlemmer, S. 2002, P&SS, 50, 1287
Giannetti, A., Leurini, S., König, C., et al. 2017a, A&A, 606, L12
Giannetti, A., Leurini, S., Wyrowski, F., et al. 2017b, A&A, 603, A33
Giannetti, A., Wyrowski, F., Brand, J., et al. 2014, A&A, 570, A65
Ginsburg, A., Henkel, C., Ao, Y., et al. 2016, A&A, 586, A50
Goldsmith, P. F. 2001, ApJ, 557, 736
Goodson, M. D., Kong, S., Tan, J. C., Heitsch, F., & Caselli, P. 2016, ApJ, 833, 274
Graninger, D. M., Herbst, E., Öberg, K. I., & Vasyunin, A. I. 2014, ApJ, 787, 74
Güver, T., & Özel, F. 2009, MNRAS, 400, 2050
Guzmán, A. E., Sanhueza, P., Contreras, Y., et al. 2015, ApJ, 815, 130
Hasegawa, T. I., Herbst, E., & Leung, C. M. 1992, ApJS, 82, 167
Hassel, G. E., Herbst, E., & Bergin, E. A. 2010, A&A, 515, A66
He, Y.-X., Zhou, J.-J., Esimbek, J., et al. 2015, MNRAS, 450, 1926
Hernandez, A. K., Tan, J. C., Caselli, P., et al. 2011, ApJ, 738, 11
Ho, P. T. P., & Townes, C. H. 1983, ARA&A, 21, 239
Hogge, T., Jackson, J., Stephens, I., et al. 2018, ApJS, 237, 27
Hugo, E., Asvany, O., & Schlemmer, S. 2009, JChPh, 130, 164302
Indriolo, N., Neufeld, D. A., Gerin, M., et al. 2015, ApJ, 800, 40
Jiménez-Serra, I., Caselli, P., Fontani, F., et al. 2014, MNRAS, 439, 1996
Johnstone, D., Boonman, A. M. S., & van Dishoeck, E. F. 2003, A&A, 412, 157
Jørgensen, J. K., Schöier, F. L., & van Dishoeck, E. F. 2004, A&A, 416, 603
Juvela, M., & Ysard, N. 2011, ApJ, 739, 63
Kamazaki, T., Okumura, S. K., Chikada, Y., et al. 2012, PASJ, 64, 29
Kauffmann, J., & Pillai, T. 2010, ApJL, 723, L7
Kong, S., Caselli, P., Tan, J. C., Wakelam, V., & Sipilä, O. 2015, ApJ, 804, 98
Kong, S., Tan, J. C., Caselli, P., et al. 2018, ApJ, 867, 94
Kramer, C., Alves, J., Lada, C. J., et al. 1999, A&A, 342, 257
Krumholz, M. R., Klein, R. I., McKee, C. F., Offner, S. S. R., & Cunningham, A. J. 2009, Sci, 323, 754
Krumholz, M. R., McKee, C. F., & Klein, R. I. 2005, ApJL, 618, L33
Lee, H. H., Herbst, E., Pineau des Forets, G., Roueff, E., & Le Bourlot, J. 1996, A&A, 311, 690
Leurini, S., Schilke, P., Menten, K. M., et al. 2004, A&A, 422, 573
Leurini, S., Schilke, P., Wyrowski, F., & Menten, K. M. 2007, A&A, 466, 215
Li, D. 2002, PhD Thesis, Cornell Univ.
Li, D., Goldsmith, P. F., & Menten, K. 2003, ApJ, 587, 262
Li, D., Kauffmann, J., Zhang, Q., & Chen, W. 2013, ApJL, 768, L5
Li, G.-X., Burkert, A., Megeath, T., & Wyrowski, F. 2016, arXiv:1603.05720
Li, S., Zhang, Q., Pillai, T., et al. 2019, ApJ, 886, 130
Lin, Y., Liu, H. B., Dale, J. E., et al. 2017, ApJ, 840, 22
Lin, Y., Liu, H. B., Li, D., et al. 2016, ApJ, 828, 32
Liu, T., Wu, Y., & Zhang, H. 2013, ApJL, 775, L2
Lu, X., Zhang, Q., Liu, H. B., et al. 2018, ApJ, 855, 9
Lubowich, D., & Pasachoff, J. M. 2010, in IAU Symp. 268, Light Elements in the Universe, ed. C. Charbonnel et al. (Cambridge: Cambridge Univ. Press), 179
Lubowich, D. A., Pasachoff, J. M., Balonek, T. J., et al. 2000, Natur, 405, 1025
Mangum, J. G., & Wootten, A. 1993, ApJS, 89, 123
McElroy, D., Walsh, C., Markwick, A. J., et al. 2013, A&A, 550, A36
McKee, C. F., & Tan, J. C. 2003, ApJ, 585, 850
Millar, T. J., Bennett, A., & Herbst, E. 1989, ApJ, 340, 906

Minamidani, T., Nishimura, A., Miyamoto, Y., et al. 2016, Proc. SPIE, 9914, 99141Z
Molinari, S., Merello, M., Elia, D., et al. 2016, ApJL, 826, L8
Molinari, S., Swinyard, B., Bally, J., et al. 2010, A&A, 518, L100
Motte, F., Bontemps, S., & Louvet, F. 2018, ARA&A, 56, 41
Müller, H. S. P., Schlöder, F., Stutzki, J., & Winnewisser, G. 2005, JMoSt, 742, 215
Neufeld, D. A., & Wolfire, M. G. 2017, ApJ, 845, 163
Pagani, L., Pardo, J. R., Apponi, A. J., Bacmann, A., & Cabrit, S. 2005, A&A, 429, 181
Pagani, L., Roueff, E., & Lesaffre, P. 2011, ApJL, 739, L35
Parise, B., Ceccarelli, C., Tielens, A. G. G. M., et al. 2002, A&A, 393, L49
Pety, J. 2005, in SF2A-2005: Semaine de l'Astrophysique Francaise, ed. F. Casoli et al. (Les Ulis: EDP Sciences), 721
Pickett, H. M., Poynter, R. L., Cohen, E. A., et al. 1998, JQSRT, 60, 883
Pineda, J. L., Goldsmith, P. F., Chapman, N., et al. 2010, ApJ, 721, 686
Planck Collaboration, Ade, P. A. R., Aghanim, N., et al. 2014, A&A, 571, A1
Pon, A., Toalá, J. A., Johnstone, D., et al. 2012, ApJ, 756, 145
Purcell, C. R., Longmore, S. N., Walsh, A. J., et al. 2012, MNRAS, 426, 1972
Ragan, S., Henning, T., Krause, O., et al. 2012, A&A, 547, A49
Rathborne, J. M., Jackson, J. M., & Simon, R. 2006, ApJ, 641, 389
Redaelli, E., Bizzocchi, L., Caselli, P., et al. 2019, A&A, 629, A15
Roberts, H., Herbst, E., & Millar, T. J. 2003, ApJL, 591, L41
Roberts, H., Herbst, E., & Millar, T. J. 2004, A&A, 424, 905
Roberts, H., & Millar, T. J. 2000, A&A, 361, 388
Rosolowsky, E. W., Pineda, J. E., Foster, J. B., et al. 2008, ApJS, 175, 509
Rygl, K. L. J., Wyrowski, F., Schuller, F., & Menten, K. M. 2013, A&A, 549, A5
Sabatini, G., Giannetti, A., Bovino, S., et al. 2019, MNRAS, 490, 4489
Sanhueza, P., Contreras, Y., Wu, B., et al. 2019, ApJ, 886, 102
Sanhueza, P., Jackson, J. M., Foster, J. B., et al. 2012, ApJ, 756, 60
Sanhueza, P., Jackson, J. M., Foster, J. B., et al. 2013, ApJ, 773, 123
Sanhueza, P., Jackson, J. M., Zhang, Q., et al. 2017, ApJ, 841, 97
Sawada, T., Ikeda, N., Sunada, K., et al. 2008, PASJ, 60, 445
Schöier, F. L., van der Tak, F. F. S., van Dishoeck, E. F., & Black, J. H. 2005, A&A, 432, 369
Schuller, F., Menten, K. M., Contreras, Y., et al. 2009, A&A, 504, 415
Shirley, Y. L. 2015, PASP, 127, 299
Shirley, Y. L., Ellsworth-Bowers, T. P., Svoboda, B., et al. 2013, ApJS, 209, 2

Sipilä, O., Harju, J., & Caselli, P. 2017, A&A, 607, A26
Sipilä, O., Hugo, E., Harju, J., et al. 2010, A&A, 509, A98
Smartt, S. J., & Rolleston, W. R. J. 1997, ApJL, 481, L47
Svoboda, B. E., Shirley, Y. L., Battersby, C., et al. 2016, ApJ, 822, 59
Tafalla, M., Myers, P. C., Caselli, P., Walmsley, C. M., & Comito, C. 2002, ApJ, 569, 815
Tan, J. C., Beltrán, M. T., Caselli, P., et al. 2014, in Protostars and Planets VI, ed. H. Beuther et al. (Tucson, AZ: Univ. Arizona Press), 149
Tan, J. C., Kong, S., Butler, M. J., Caselli, P., & Fontani, F. 2013, ApJ, 779, 96
Tan, J. C., Kong, S., Zhang, Y., et al. 2016, ApJL, 821, L3
Tang, X. D., Henkel, C., Menten, K. M., et al. 2018, A&A, 609, A16
Tatematsu, K., Liu, T., Ohashi, S., et al. 2017, ApJS, 228, 12
Tielens, A. G. G. M. 2013, RvMP, 85, 1021
Urquhart, J. S., König, C., Giannetti, A., et al. 2018, MNRAS, 473, 1059
Urquhart, J. S., Moore, T. J. T., Csengeri, T., et al. 2014, MNRAS, 443, 1555
van der Tak, F. F. S., Black, J. H., Schöier, F. L., Jansen, D. J., & van Dishoeck, E. F. 2007, A&A, 468, 627
Vastel, C., Phillips, T. G., Caselli, P., Ceccarelli, C., & Pagani, L. 2006, RSPTA, 364, 3081
Walmsley, C. M., & Ungerechts, H. 1983, A&A, 122, 164
Wang, K. 2018, RNAAS, 2, 52
Wang, K., Zhang, Q., Testi, L., et al. 2014, MNRAS, 439, 3275
Wang, K., Zhang, Q., Wu, Y., Li, H.-b., & Zhang, H. 2012, ApJL, 745, L30
Wang, S., Ren, Z., Li, D., et al. 2020, arXiv:2007.05229
Watanabe, N., Kimura, Y., Kouchi, A., et al. 2010, ApJL, 714, L233
Watson, W. D. 1976, RvMP, 48, 513
Wenger, T. V., Balser, D. S., Anderson, L. D., & Bania, T. M. 2018, ApJ, 856, 52
Wienen, M., Wyrowski, F., Schuller, F., et al. 2012, A&A, 544, A146
Willacy, K., Langer, W. D., & Velusamy, T. 1998, ApJL, 507, L171
Wilson, T. L., & Rood, R. 1994, ARA&A, 32, 191
Wyrowski, F., Güsten, R., Menten, K. M., et al. 2016, A&A, 585, A149
Wyrowski, F., Güsten, R., Menten, K. M., Wiesemeyer, H., & Klein, B. 2012, A&A, 542, L15
Yamamoto, S. 2017, Introduction to Astrochemistry: Chemical Evolution from Interstellar Clouds to Star and Planet Formation (Tokyo: Springer)
Yuan, J., Wu, Y., Ellingsen, S. P., et al. 2017, ApJS, 231, 11
Zhang, Q., Wang, K., Lu, X., & Jiménez-Serra, I. 2015, ApJ, 804, 141
Zhang, Q., Wang, Y., Pillai, T., & Rathborne, J. 2009, ApJ, 696, 268